MULTIPHASE FLOW

Multi-Phase Fluid Hammer: Modeling, Experiments and Simulations

Marcos Lema

Environmental and Applied Fluid Dynamics Department, von Karman Institute for Fluid Dynamics, Belgium, lema@vki.ac.be

Supervisor: Patrick Rambaud

Associate Professor, Environmental and Applied Fluid Dynamics Department, von Karman Institute for Fluid Dynamics, Belgium, rambaud@vki.ac.be

Supervisor: Jean-Marie Buchlin

Associate Professor, Environmental and Applied Fluid Dynamics Department, von Karman Institute for Fluid Dynamics, Belgium, buchlin@vki.ac.be

University Supervisor: Fernando López Peña

Professor, Naval and Oceanic Engineering Department, University of A Coruña, Spain, flop@udc.es

Abstract

The operation of spacecraft propulsion systems is regularly faced with adverse fluid hammering effects during the priming phase. This manoeuvre is done by fast opening of an isolation valve and the classical water hammer taking place involves multiphase phenomena, such as cavitation and absorption/desorption of a non-condensable gas. Due to the lack of experimental studies modelling the spacecraft's hardware, the physical models implemented in the numerical codes cannot be validated properly when computing the corresponding overpressures during priming with a multiphase flow. Hence, a new experimental facility reproducing all the physical phenomena taking place in the propellant lines during the priming has been built, and the experimental data is used to validate the physical models. Two CFD codes are used to model the flow configuration and the numerical results presented as X-t diagrams reveal a complex multilayer configuration prior to the fluid hammer occurrence, which certainly affects the speed of sound in the fluid and changes the pressure surge produced during priming.

Keywords: Multi-phase flow, fluid hammer, water hammer, cavitation, absorption, desorption, priming, spacecraft propulsion.

1. Introduction

When a satellite is launched to the space, its propulsion system is initially inactive, with the liquid propellant confined in the tanks and isolated from the nozzles and catalyst beds by three valves, as sketched in figure 1. Once the spacecraft has been ejected from the launcher vehicle, the evacuated propellant lines are filled with pressurized liquid propellant. This maneuver is called "priming" and is carried out by the fast opening of a pyrotechnic isolation valve. This induces a fluid hammer pressure front that may turn out to be critical if the corresponding overpressures are not correctly taken into consideration in the pipe line and sub-system dimensioning. Furthermore, since the propellant lines are initially vacuum pumped or filled with a non-condensable gas (NCG) at low pressure, the classical water hammer includes various multiphase phenomena, such as cavitation and boiling front. Finally, the driving pressure gas can be absorbed into the liquid propellant during storage and can desorb during the priming process.

Due to the complexity of these multiphase phenomena occurring in spacecraft hardware, there are very few literature references describing experiments with all the specifications of the above configuration, and which are necessary for a proper validation of the physical models implemented in the CFD codes.

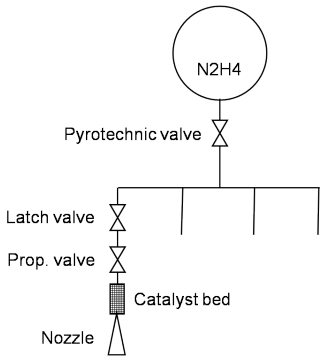

Figure 1: Monopropellant propulsion system configuration

Nowadays, various numerical codes are able to accurately predict the liquid compressibility effects when computing a single-phase fluid hammer but they still need to be extended and calibrated for cases with cavitation and two-phase flows. Furthermore, the numerical treatment of a dissolved NCG in the liquid phase needs to be improved. In both cases, the existence of a well documented experimental database is mandatory for the improvement and validation of these physical models. Even if it is possible to find numerous studies dedicated to the fluid hammer, the references dealing with the priming process are not so numerous and the data available is not sufficient for validation purposes.

A first group of reference deals with the explosive decomposition of hydrazine due to the adiabatic compression produced at the liquid propellant front. In these studies, such as Briels and Hollenbaugh[1], [2], Hutchinson and Schmitz[3] and Bunker et al.[4], the purpose was not to study priming directly, but the adiabatic compression that may be a consequence of it. In fact, liquid hydrazine is known to undergo exothermic decomposition when the liquid is heated under quasistatic conditions. These studies used both U-shaped tubes or fast opening valves to create the pressure raise compressing the hydrazine, but the test conditions have been poorly described. Bunker et al.[4] used, to our knowledge, high speed imaging for the first time to visualize the hydrazine liquid front, capturing the formation of foam at the gas-liquid interface. The authors described this foam as nitrogen bubbles surrounded by thin layers of liquid hydrazine. When the foam experiences a compression due to the accelerated liquid column, the nitrogen bubbles are heated adiabatically and the generated heat is transferred to the hydrazine layer.

A second group of references are specifically dedicated to the analysis of flow transients during the priming process, using both experimental and theoretical/numerical approaches, on simplified test configurations or the whole propulsion system, where the authors tried to evaluate the risk of adiabatic detonation or the integrity of the piping system facing water hammer pressure surges. In this category we can list the studies from Yaggy [5], Prickett et al.[6] Molinsky[7], Martin et al.[8], Joh et al.[9] and Morgan[10]. The main conclusions of these studies are: unsteady friction plays an important role, the two-phase phenomena are directly linked to the pressure surge amplitude and water can replaced MMH (monomethylhydrazine) as test fluid, producing pressure surges higher than the MMH and is, therefore, conservative. Several authors attempted to model the priming process using dedicated numerical tools, such as Lin and Baker[11], Navickas et al.[12], Ounougha and Colozzi[13], Leca et al.[14] and Hern[15]. In most of the cases, the simulations have been done with 1D simulations where two-phase phenomena were not taken into account.

Finally, two references are closely related to the present study, Gibek and Maisonnneuve[16] and Lecourt and Steelant[17], where the main objective were to model experimentally the priming process taking place in satellites and to create an experimental database for validation purposes. Gibek and Maisonnneuve used both real propellants and water, while Lecourt and Steelant used only inert fluids. The authors of these studies concluded the existence of a boiling front from the start, resulting in a local two-phase mixture of vapour and liquid. Furthermore, the NCG initially present in the test pipe get compressed when the valve opens and the liquid front travels downstream. Since this compression occurs very fast, it is mainly adiabatic at the boundaries, producing an intense mixing and heat transfer at the multiphase liquid-vapour/NCG front. Lecourt and Steelant[17] also studied in detail the evolution for the first pressure peak, where a multiple step evolution before reaching the maximum pressure value was observed, and gave some hypothesis to explain this behaviour.

2. Objectives

The aim of this work is to study the fluid hammer phenomenon in a confined environment with both experimental and numerical approaches. The experimental results come to complete the data already available in the literature, but using an experimental set-up which can reproduce all the physical phenomena taking place in the propellant lines during prim-

ing. The numerical investigation is done with 1D and 3D CFD codes and their results are compared against the experimental data. This comparison will allow the improvement and validation of the physical models implemented in the codes.

3. Experimental facility

A new experimental facility has been built at the von Karman Institute and includes all the elements of a satellite propulsion system directly involved in the fluid hammer occurrence: a pressurized liquid tank, a fast opening valve (FOV) and a given length of pipe line. The main objective during the design phase was to conceive a facility without singular elements such as elbows and T-junctions upstream the FOV, and with the same inner diameter in every flow conduction. It is well known that these geometrical singularities create secondary pressure waves, which complicate the general pressure measurements interpretation. Furthermore, the absence of these elements simplify considerably the numerical modelling of the facility and, thus, the results validation.

The facility layout is shown in figure 2, which is intended to be clamped on a vertical wall. The main components are a pressure vessel, a fast opening valve (FOV) and a given length of the propellant line, referred to as "test element" hereafter. Three test element configurations are used: straight, 90° elbow and T-bifurcation. The test elements are made with the same titanium tube of $1/4''$ and following the same construction rules used for aerospace applications. The facility also includes a vacuum system to set the test conditions (test element initially vacuum pumped or filled with a NCG gas at low-pressure). The characterization of the wave front induced by the fluid hammer is achieved through interchangeable measurement modules attached to the bottom end of the test element. Two types of measurement modules are proposed in this study: an instrumented module with unsteady pressure and temperature transducers and a transparent module made out of quartz for flow visualization with high speed imaging. The test vessel is a spherical accumulator that can mount an elastic membrane and it is equipped with an ultrasonic transducer to measure the speed of sound in the liquid. The purpose of the membrane is to avoid the absorption of the NCG during the liquid pressurization, allowing to run experiments with "pure" liquid. These test results provide very useful information to understand how the dissolved gas affects the fluid hammer mechanism. Furthermore, since the working liquid is already saturated with air in standard conditions during storage, the fluid needs to be deaerated to run experiments without any dissolved gas. The liquid deaeration is done by means of a depressurization process using a second accumulator, called deareation vessel, connected to the vacuum pump. The dissolved gas is removed by keeping the liquid in a low-pressure atmosphere. This facility allows to work with inert fluids and nitrogen as driving pressure gas.

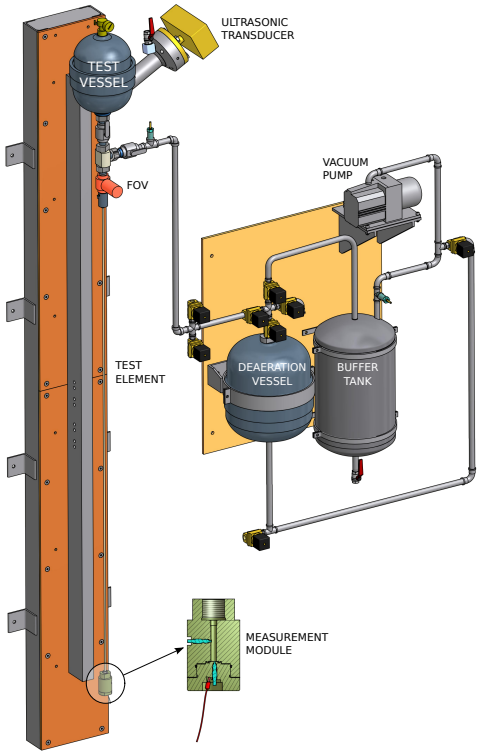

Figure 2: Experimental facility layout

4. Numerical tools

The numerical study is carried out with two commercial codes: EcosimPro/ESPSS and CFD-ACE+. EcosimPro is a 1D simulation tool, object-oriented and capable of computing steady state and transient physical processes. The code employs the European Space Propulsion System Simulation (ESPSS) library [18], which is needed to model all aspects of a functional propulsion system. This is achieved by four

libraries: **Fluid_properties** library, a database with the properties of most of the fluids used for aerospace applications, **Fluid_flow_1d** library, which allows 1D transient simulation of two-fluid, two-phase flows, and **Tanks** and **Turbo_Machinery** library, to model tanks, pumps, turbines and compressors. Based on the simplified facility, the schematic view shown in figure 3 was done in EcosimPro with generic elements from the ESPSS library. The model configuration is quite straightforward with this code, where the main parameters that the user needs to set are the initial conditions of pressure and temperature in every flow element, the mass fraction of NCG dissolved in the liquid and the valve opening law.

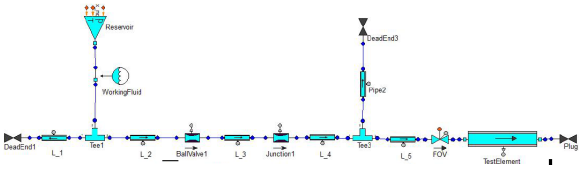

Figure 3: Schematic view of the simplified facility under EcosimPro

The second numerical code used in this study is CFD-ACE+, a general 3D computational fluid dynamics and multiphysics solver. This commercial code has been updated with a full cavitation module, which allows to work with a homogeneous mixture of liquid, vapour and NCG (with absorption and desorption), to model non-isothermal flows and liquid compressibility for fluid hammer simulations. In this module, cavitation is solved with a method where turbulence is taken into consideration in the bubble growth and collapse computation [19]. Regarding the liquid compressibility, the module proposes several models for different liquids. There are two models for water compressibility: Rouleau [20] and Elansary [21], one model for oil by Rouleau, and two models proposed by Onera for ethanol and MMH.

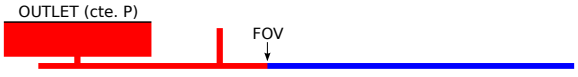

Figure 4: 2D domain and initial conditions configuration for the CFD computations

The numerical simulations with CFD-ACE+ are carried out on a 2D domain shown in figure 4, which includes the liquid tank and the geometry of the piping network. The test conditions are set separately upstream and downstream the valve, as sketched in figure 4, where red colour represents the pressurized liquid, and blue colour the vacuum pumped test element. The valve opening process is done using the grid deformation capability of the code.

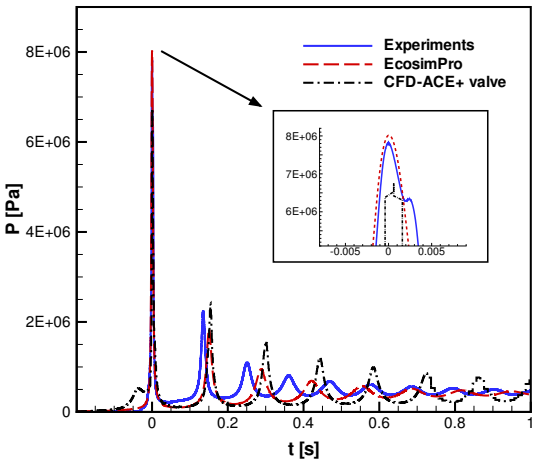

Figure 5: Experimental and numerical results comparison with test conditions $P_t = 0.4\,MPa$ and $P_p = 10\,kPa$

Figure 5 shows the comparison of preliminary experimental measurements with the data obtained with the numerical codes EcosimPro/ESPSS and CFD-ACE+ modelling the same set-up. The comparison with EcosimPro/ESPSS results gives a reasonably good agreement for the first pressure peak, although the computed pressure level is slightly higher. Furthermore, even if the successive pressure spikes are always higher in the experiments, the damping of the successive pressure peaks is also very consistent with the experimental data. The CFD results show a slightly lower first pressure surge but higher successive pressure peaks. On the other hand, the time delay between peaks computed numerically with both codes is rather similar. The fact that the numerical codes are not consistent with the pressure level estimation, and looking to the frequency of the peaks , it looks like the liquid velocity is predicted too low. This might be due to the difficulty of evaluating the friction for an accelerated, multiphase flow. On top of that, the speed of sound modeling a liquid/gas mixture needs to be improved in both codes, since this value looks over-predicted. Anyway, these first results show that both codes are already able to compute the fluid hammer phenomenon during priming, providing a good estimation of the first pressure surge.

5. 2D presentations of the results: X-t diagrams

Although the numerical codes are not yet fully validated when modelling the priming operation, they are already powerful tools to analyse the fluid hammer phenomenon. Therefore, EcosimPro/ESPSS has been chosen to validate the facility design. In this case, the test conditions are set to $P_t = 2\,MPa$ and $P_p = 1\,kPa$, using water and nitrogen as working fluids in the $2\,m$ straight test element configuration. Since the pipe flow can be assumed one-dimensional, the numerical results can be presented using X-t diagrams. These diagrams allow temporal and spatial representation of the flow in the same graph, where the x-axis corresponds to the position along the test element, and the time is plotted in the y-axis. Figure 6 shows the X-t diagram obtained with the EcosimPro results, where the colour levels represent the pressure amplitude. The pressure evolution at the bottom end of the test element P_{wh} is plotted at the right side of the figure for a better understanding.

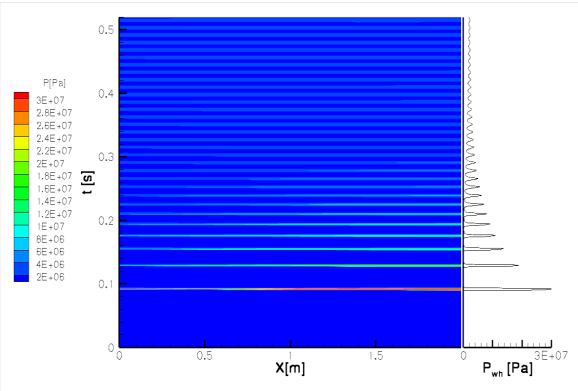

Figure 6: X-t diagram for the pressure variable

According to the Joukowsky equation, the kinematic energy is converted into pressure, leading to a pressure peak of $30\,MPa$. In the X-t diagram the pressure raise produced by the fluid hammer appears as parallel stripes, whose thickness is equivalent to the pressure spike bandwidth at each location of the test element. The stripes colour intensity decreases as one moves upwards on the diagram (in time), which shows, as in the 1D pressure evolution diagram, that the pressure spikes are damped in time until its complete attenuation. On the other hand, the pressure amplitude also decreases from right to left (in space), showing that the pressure raise decreases while travelling along the pipe. Thus, the 2D map is a valuable tool of analysis, providing information that can not be obtained with a 1D history recording.

6. Multiphase behaviour of the liquid front

The fluid hammer produced in the present flow configuration involves several multiphase phenomena, including vaporous and gaseous cavitation. Vaporous cavitation occurs when the local pressure drops below the vapour pressure and gaseous cavitation occurs when the local pressure drops below the saturation pressure of the NCG dissolved in the liquid[22]. That is why the most complex features taking place occur when the liquid front faces the vacuum conditions in the test element, i.e between the opening of the FOV and the arrival of the liquid front at the bottom end. In order to identify the physical phenomena involved, two parameters are proposed: the void fraction, α, which expresses the fraction of the gaseous phase (vapour and NCG) in a given volume of fluid, and the NCG mass fraction, x_{nc}.

$$\alpha = \frac{V_{gas}}{V_{total}} \tag{1}$$

$$x_{nc} = \frac{m_{nc}}{m_{total}} \tag{2}$$

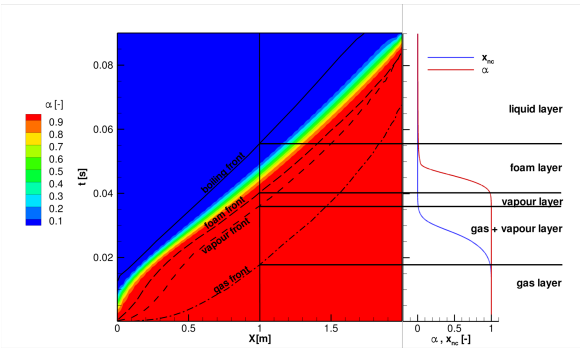

Figure 7: X-t diagram for the void fraction before the first impact

In equation 2, m_{nc} refers only to the NCG in evolved state. Therefore, when $\alpha = 1$, the volume is full of gas (vapour or NCG) and when $x_{nc} = 1$ the volume is full of NCG in gaseous state.

Figure 7 shows the X-t diagram coloured with the void fraction, together with a side graph with the void fraction and the NCG mass fraction history obtained at half-length of the test element ($X = 1\,m$). The time interval represented in this diagram goes from the opening of the FOV until the impact of the liquid front at the bottom end ($0 < t < 0.09\,s$). According to this

graph, five different layers can be distinguished when moving upstream in the graph at $X = 1\,m$. Initially, there is only the presence of NCG ($x_{nc} = 1$), creating the **gas layer**. Later, a thick **gas+vapour layer** appears, where the NCG is gradually evacuated and replaced by the vapour phase ($\alpha = 1$ and $x_{nc} < 1$). The third layer contains only vapour: **vapour layer** ($\alpha = 1$ and $x_{nc} = 0$). In the fourth layer, droplets of liquid start to appear ($\alpha < 1$), generating the **foam layer**. Finally, in the fifth layer there is only liquid phase ($\alpha = 0$), named **liquid layer**. As the liquid layer approaches the bottom end, the pressure increases, which makes the vapour condensate and the NCG dissolve into the liquid.

This multi-layer structure with variable composition basically reflects the consecutive multi-phase flow phenomena taking place during priming. The sudden exposure of the liquid to vacuum initiates its vaporization or boiling as it falls suddenly below the vapour line. The vaporization process takes place over a finite layer thickness where the liquid transforms gradually towards a pure vapour. Within this layer, liquid and vapour coexist and form a foam. Due to their large density ratio, the vapour is expelled upstream of the foam front where it eventually mixes up with the NCG. This does not happen immediately at the foam front but slightly upstream of it, at the vapour layer front. The priming or gas front indicates the most downstream location of the upcoming water hammer effect.

7. Fluid hammer mechanism during priming

Since the first impact of the liquid front is in the origin of the pressure surge, the understanding of the first pressure spike may give insight in the wave propagation and dissipation mechanism. To do so, the pressure evolution in the 50 nodes in which the test element was discretized during the computations with EcosimPro/ESPSS has been plotted in a single graph, and zooming in the first pressure spike ($0.09 < t < 0.094$), as shown in figure 8. The corresponding pressure raise for node 1, 25 and 50 has been highlighted with thicker lines for the sake of clarity, where node 1 is situated right after the FOV, node 25 is at half-length of the test element and node 50 gives the highest pressure surge obtained at the forward end.

When the FOV opens, the liquid front travels along the pipe, arriving at $t = 0.09\,s$ at the bottom end. Since the test element has a length of $2\,m$, the average travelling velocity of the liquid front is $22.22\,m/s$. The front velocity drops to zero after the impact and the kinetic

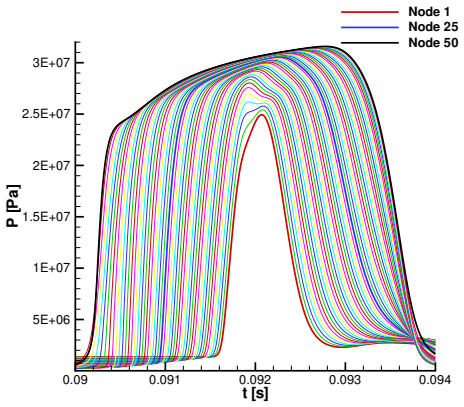

Figure 8: First pressure peak recorded in the 50 nodes of the test element

energy of the flow is converted into pressure energy. In order to estimate the pressure raise, let us assume that the density and the sound velocity in the liquid are constant and equal to $998\,kg/m^3$ and $1482\,m/s$ respectively (distilled water at $20°C$). With these values, the Joukowsky equation gives a pressure raise equal to $\Delta P = 32.8\,MPa$. This value is consistent with the one obtained numerically, $P_{wh} = 31.3\,MPa$, recorded at the bottom end during the first pressure peak. This flow information, pressure raise and null flow velocity, is now transmitted upstream at the speed of sound as a pressure wave ("PW1"). One can observe that, according to figure 8, there is a time delay of approximately $\Delta t_1 = 0.0014\,s$ between the pressure raise at the bottom end (thick black line) and the one produced at the valve location (thick red line). Taking into account that the test element is $2\,m$ long, this gives a velocity of $1429\,m/s$, which is also consistent with the theoretical value.

Figure 8 also shows that the pressure raise produced has two slopes. First, there is an abrupt, quasi-instantaneous, pressure augmentation until $P_{wh} = 23\,MPa$. Front this point, the pressure continues increasing at a lower rate, with the peak at $P_{wh} = 31.3\,MPa$. An attempt to explain this behaviour may be offered with figure 9, which shows the liquid front velocity in each node. As it was already said, around $t = 0.09\,s$, when the liquid front reaches the bottom end, the flow velocity drops to zero, and the water hammer taking place increase the liquid pressure. The pressure wave starts travelling upstream given the new flow information to the liquid flow, i.e. null velocity and P_{wh}. But while this is happening, there is part of the liquid column that is still travelling downstream,

which explains the continuous pressure increase at the bottom end. In other words, since upstream pressure is always greater than downstream pressure before the impact, the surge pressure will continuously increase in order to bring fluid flow to rest[11].

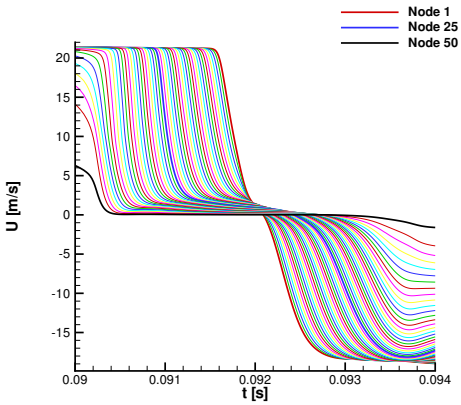

Figure 9: Liquid front velocity computed during the first pressure peak

At $t = 0.092\,s$ the pressure wave reaches the FOV and shortly after the tank. This fact imposes a new pressure condition to the flow, which is P_t. Such a change occurs because the tank has an infinite volume compared to the one of the test element. The pressure condition set by the tank travels now downstream as a expansion wave ("EW1"). Under these circumstances, and before EW1 arrives to the bottom end, there is a high pressure gradient in the fluid ($P_t <<< P_{wh}$), which makes the liquid column to move towards the tank for $t > 0.092\,s$, as it is observed in figure 9 (negative velocity values due to the upstream direction). This is possible because the liquid has an elastic behaviour with variable density, as figure 10 shows, causing a higher negative velocity in the fluid particles close to the valve, around $-19\,m/s$, than those close to the bottom end. Furthermore, this difference is more pronounced after node 25, showing in the last node a maximum negative velocity of nearly $-2\,m/s$.

While the liquid column starts to move upstream, the pressure starts to drop and, approximately at $t = 0.0928$, the fluid particles at the bottom end start moving upstream. The movement of the whole liquid column is possible due to the growing of the void fraction downstream. In fact, the liquid column leaves a foam pocket behind, which is clearly identified in figure 12. The colour map of this X-t diagram represents the void fraction and, according to the side graph plotted in the same figure, the foam pocket consists of a mixture of only liquid and vapour, as no trace of NCG is predicted after the arrival of EW1. Based on the X-t diagram of figure 12, we observe that this first foam pocket reaches the coordinate $X = 1.3\,m$ during the EW1 reflection.

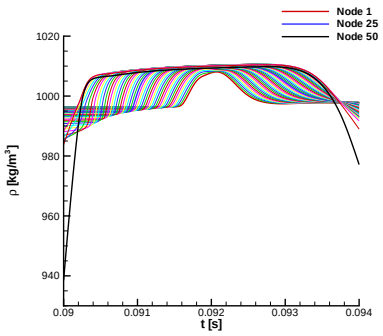

Figure 10: Liquid front density computed during the first pressure peak

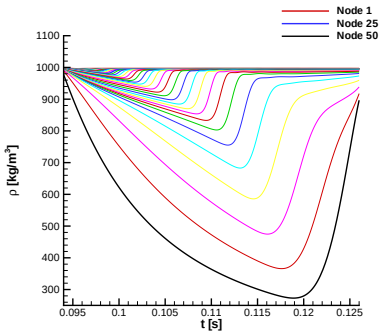

Figure 11: Liquid front density computed after the arrival of EW1

The density variation after the first peak shown in figure 11 is also related to the foam pocket, where the density value shows a pronounced decrease in the nodes affected by the pocket growth. Finally, between $0.11\,s < t < 0.12\,s$ the fluid density starts to increase (figure 11) and the void fraction to decrease until the collapse of the foam pocket. This phenomenon generates a new impact of the liquid column against the bottom wall, producing a second pressure raise "PW2", and the whole process starts all over again. Each pressure spike is attenuated due to viscous dissipation, driving to the complete extinction of the fluid hammer phenomenon after $0.8\,s$.

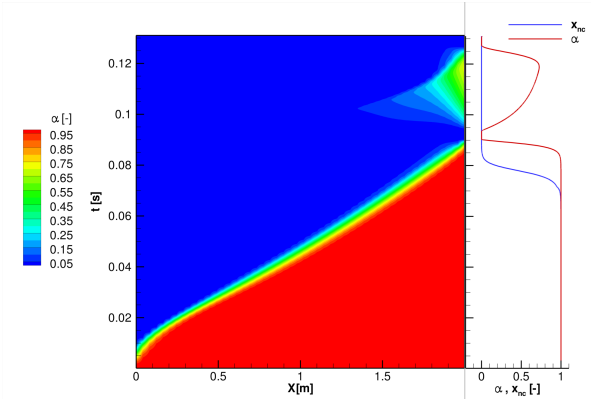

Figure 12: X-t diagram: foam pocket formation during the first expansion reflection

8. Summary

This work describes both experimental and numerical approaches to study the priming process taking place in satellites. The experimental facility proposed in this study reproduces the fluid hammer produced during priming, which consists of a pressurized liquid tank, a fast opening valve and a given length of propellant line, which is vacuum pump before launching a test.

Two numerical codes are used for the numerical approach: EcosimPro and CFD-ACE+. Both codes have been updated respectively with the ESPSS library and the full cavitation module, which allow the modelling of fluid compressibility with a homogeneous mixture of liquid, vapour and NCG. The comparison of the experimental and the numerical results has shown a reasonable good prediction of the first pressure peak. On the other hand, some effort is still needed in the prediction of the second and successive peaks with both codes.

The X-t processing has shown the multiphase nature of the liquid front, with the generation of multiple layers at the liquid front before the impact at the bottom end. A detailed analysis of the speed of sound is now necessary in each layer, and needs to be taken into account to model correctly the pressure peak level and the time delay between successive peaks.

Finally, the analysis of the fluid hammer mechanism has shown a complex behaviour of the flow and the pressure waves during the first pressure peak. The displacement of the liquid column upstream, the generation of a foam pocket at the bottom end and the collapse of this pocket is in the origin of the successive pressure peaks produced in the flow.

Acknowledgments

This study is supported by the European Space Agency through the GSTP activity AO/1-6210/09/NL/CP.

References

[1] O. M. Briles, R. P. Hollenbaugh, Adiabatic compression testing of hydrazine, in: AIAA/SAE 14th Joint Propulsion Conference, Las Vegas, USA, 1978.

[2] O. Briles, D. Hagemann, F. Benz, T. Farkas, Explosive decomposition of hydrazine due to rapid gas compression, Tech. rep., White Sands Test Facility (1985).

[3] F. E. Hutchinson, H. D. Schmitz, Adiabatic compression phenomena in hydrazine propulsion systems, in: 20th AIAA/SAE/ASME joint propulsion conference, 1984.

[4] R. L. Bunker, D. L. Baker, J. H. S. Lee, Explosive decomposition of hydrazine by rapid compression of a gas volume, Tech. rep., Johnson Space Center, White Sands Test Facility (1990).

[5] K. L. Yaggy, Analysis of propellant flow into evacuated and pressurized lines, in: 20th AIAA/SAE/ASME Joint Propulsion Conference and Exhibit, 1984.

[6] R. P. Prickett, E. Mayer, J. Hermal, Water hammer in a spacecraft propellant feed system, Journal of Propulsion and Power 8 (3) (1992) 592–597.

[7] J. Molinsky, Water hammer test of the seastar hydrazine propulsion system, in: 33rd AIAA/ASME/SAE/ASEE Joint Propulsion Conference & Exhibit, 1997.

[8] T. Martin, L. Rockwell, C. Parish, Test and modeling of the mars '98 descent propulsion system waterhammer, in: 34rd AIAA/ASME/SAE/ASEE Joint Propulsion Conference & Exhibit, 1998.

[9] C. Y. Joh, K. D. Park, Pressure surge analysis and reduction in the kompsat propellant feed system, in: Proceedings KORUS 2000. The 4th Korea-Russia International Symposium on Science and Technology, 2000.

[10] M. J. Morgan, Pressure transient characterization test for star-2 propulsion system fuel manifold, in: 40th AIAA/ASME/SAE/ASEE Joint Propulsion Conference and Exhibit, 2004.

[11] T. Y. Lin, D. Baker, Analysis and testing of propellant feed system priming process, Journal of Propulsion and Power 11 (3) (1995) 505–512.

[12] J. Navickas, W. C. Rivard, A. R. Porter, D. L. Baker, K. A. Rathgeber, Structural pressures developed during fill of evacuated systems, in: AIAA, Fluid Dynamics Conference, 1996.

[13] L. Ounougha, F. Colozzi, Correlation between simulations and experiments on water hammer effect in a propulsion system, in: Proceedings of Second Eurpean Spacecraft Propulsion Conference, 1997.

[14] C. Leca, P. Boh, Mon and mmh pressure surges for a simplified propellant feed system, in: proceedings of 3rd international conference on spacecraft propulsion, Cannes, France, 2000.

[15] H. C. Hearn, Development and application of a priming surge analysis methodology, in: 41st AIAA/ASME/SAE/ASEE Joint Propulsion Conference & Exhibit, 2005.

[16] I. Gibek, Y. Maisonneuve, Waterhammer tests with real propellants, in: proceedings of 41st AIAA/ASME/SAE/ASEE Joint Propulsion Conference & Exhibit, Tucson (AZ), USA, 10-13 July, no. 2005–4081, 2005.

[17] R. Lecourt, J. Steelant, Experimental investigation of water hammer in simplified feed lines of satellite propulsion systems, Journal of Propulsion and Power 23(6) (2007) 1214–1224.
[18] J. Moral, R. Perez-Vara, J. Steelant, M. de Rosa, Espss simulation platform, in: proceedings of 2010 Space Propulsion conference, San Sebastian, Spain, 2010.
[19] A. K. Singhal, M. M. Athavale, H. Li, Y. Jiang, Mathematical basis and validation of the full cavitation model, Journal of Fluids Engineering 124 (2002) 617–624.
[20] E. Holmboe, W. Rouleau, The effect of viscous shear on transients in liquid lines, ASME Journal of Basic Engineering 1 (1967) 174–180.
[21] A. S. Elansary, W. Silva, M. H. Chaudhry, Numerical and experimental investigation of transient pipe flow, Journal of Hydraulic Research 32 (1994) 689–706.
[22] A. S. Tijsseling, Fluid-structure interaction in liquid-filled pipe systems: a review, Journal of Fluids and Structures 10 (1996) 109–146.

Numerical modeling and experimental investigation of fine particle coagulation and dispersion in dilute flows

Bart Janssens

Department of Mechanical Engineering, Royal Military Academy, Belgium, bart.janssens@rma.ac.be

Supervisor: Tony Arts

Professor, Turbomachinery and Propulsion Department, von Karman Institute for Fluid Dynamics, Belgium, arts@vki.ac.be

Supervisor: Walter Bosschaerts

Professor, Department of Mechanical Engineering, Royal Military Academy, Belgium, walter.bosschaerts@rma.ac.be

University Supervisor: Karim Limam

Professor, Laboratoire d'Étude des Phénomènes de Transfert et de l'Instantanéité, France, klimam01@univ-lr.fr

Abstract

In this work, a numerical model will be developed to study the behavior of fine and ultra fine particles under conditions typical for air pollution problems. The particles considered are much heavier than the surrounding fluid, and can have sizes ranging from 5 nm to 10 μm. Effects of inter-particle collisions and coagulation will be included in the model.

The current discussion focuses on the development of the solver for the incompressible Navier-Stokes equations, using the SUPG finite element technique and with an implementation that makes use of a Domain Specific Embedded Language.

Finally, some preliminary PIV measurements, to be used for validation of the simulated flow field, will also be presented.

Keywords: Multiphase flow, Disperse flow, coagulation, LES, nanoparticles

1. Introduction

One of the major factors in determining air quality is the level of pollution in the form of particles. In general, particles with an aerodynamic diameter inferior to 10 μm can penetrate into the human body, and constitute a potential health risk [1]. Recently, the additional risks of nanoparticles have received much attention [2], so we will study particles in a range from about 5 nm to 10 μm. The goal of the present work is to arrive at a contribution to the numerical modeling of particle-laden flow, where the behavior of ultra fine particles is taken into account, as well as inter-particle collision and coagulation. This will be done in two phases: a model development phase, followed by an application phase. The target applications include flows in confined spaces that can be modeled using CFD. Particle loading should be such that the flow can be considered dilute, i.e. particle dynamics are dominated by the flow rather than inter-particle collisions.

So far, we focused on the implementation of a Finite Element Method with SUPG stabilization [3]. This was done within the framework of a Domain Specific Embedded Language, which greatly simplifies the implementation of Petrov-Galerkin approximations. The method can be compared to FEniCS [4] and Life [5]. OpenFOAM also has a similar language to express finite volume problems [6]. The following paragraphs will show how our framework was used to implement the SUPG scheme.

Experimental work was also started with PIV measurements to be used for flow model validation. The

first results are presented in paragraph 3.

2. Numerical model

The numerical method for solving the basic flow equations uses a Finite Element discretization, stabilized using the SUPG scheme. This allows the use of a single grid for the pressure and velocity. The method is detailed in [3]. What follows is a brief overview of the procedure, followed by details of the implementation using a Domain Specific Embedded Language (DESL).

2.1. Finite Element discretization

We consider the incompressible Navier-Stokes equations for conservation of mass and momentum:

$$\nabla \cdot \mathbf{u} = 0 \tag{1}$$

$$\frac{\partial \mathbf{u}}{\partial t} + (\mathbf{u} \cdot \nabla)\,\mathbf{u} + \frac{\nabla p}{\rho} - \nu \nabla^2 \mathbf{u} = \mathbf{0} \tag{2}$$

The equations are transformed to the weak formulation and PSPG, SUPG and bulk stabilization terms are applied, weighted by the respective coefficients τ. For the time discretization, a forward Euler method is used here for clarity, yielding the following semi-discrete weak formulation:

$$\int_\Omega \omega \nabla \cdot \mathbf{u}^{n+1} \mathrm{d}\Omega + \int_\Omega \tau_{\mathrm{PSPG}} \nabla\omega \cdot \left(\frac{\mathbf{u}^{n+1} - \mathbf{u}^n}{\Delta t} + \left(\mathbf{u}^{n+1} \cdot \nabla\right)\mathbf{u}^{n+1} + \frac{\nabla p^{n+1}}{\rho} \right) \mathrm{d}\Omega = 0 \tag{3}$$

$$\int_\Omega \left(\omega + \tau_{\mathrm{SUPG}} \nabla\omega \cdot \mathbf{u}^{n+1}\right) \left(\frac{\mathbf{u}^{n+1} - \mathbf{u}^n}{\Delta t} + \left[(\mathbf{u} \cdot \nabla)\,\mathbf{u} + \frac{\nabla p}{\rho} - \nu \nabla^2 \mathbf{u} \right]^{n+1} \right) \mathrm{d}\Omega + \int_\Omega \tau_{\mathrm{BULK}} \nabla\omega \left(\nabla \cdot \mathbf{u}^{n+1}\right) \mathrm{d}\Omega = \mathbf{0} \tag{4}$$

The superscripts n and $n+1$ indicate the solution at two subsequent time steps, ω represents the weight function and Ω is the problem domain.

A space discretization is now obtained by splitting the domain into a number of smaller elements Ω_k over which we define shape functions $\mathbf{N}$, which we write here as a row vector containing a weight for each element node. We can then multiply $\mathbf{N}$ with a column vector of nodal values to obtain an interpolated value for a variable. This interpolation scheme is applied to the unknowns $\mathbf{u}$ and p, resulting in an equation that depends on the unknown nodal values. Furthermore, the weight function ω is chosen to be equal to the shape function and is written in each node, resulting in a number of equations equal to the number of nodes. Applying this procedure to the weak forms (3) and (4) yields an equation that can be written in matrix form for each element, which we define as follows:

$$\frac{1}{\Delta t} T_e \left(\mathbf{x}_e^{n+1} - \mathbf{x}_e^n \right) + A_e \mathbf{x}_e^{n+1} = \mathbf{0} \tag{5}$$

The elemental vector of unknowns $\mathbf{x_e}$ is arranged as follows:

$$\mathbf{x_e}^n = \begin{bmatrix} p_0^n & \dots & p_m^n & \left(u_0^n\right)_0 & \dots & \left(u_0^n\right)_m & \left(u_1^n\right)_0 & \dots & \left(u_1^n\right)_m & \left(u_2^n\right)_0 & \dots & \left(u_2^n\right)_m \end{bmatrix}^\intercal \tag{6}$$

Here, m is the number of nodes for an element. The structuring of the vector of unknowns also allows us to subdivide the element matrices T_e and A_e as follows (showing only A_e and considering three velocity components):

$$A_e = \begin{bmatrix} A_{pp} & A_{pu_0} & A_{pu_1} & A_{pu_2} \\ A_{u_0 p} & A_{u_0 u_0} & A_{u_0 u_1} & A_{u_0 u_2} \\ A_{u_1 p} & A_{u_1 u_0} & A_{u_1 u_1} & A_{u_1 u_2} \\ A_{u_2 p} & A_{u_2 u_0} & A_{u_2 u_1} & A_{u_2 u_2} \end{bmatrix} \tag{7}$$

Each element of this matrix is an $m \times m$ sub matrix for which the rows correspond to the equations at each element node for the variable in the first subscript and the columns represent the nodal contributions for the variable in the second subscript. Comparing this structure with the weak forms (3) and (4) allows us to define each matrix, after applying the interpolation procedure:

$$A_{pu_i} = \int_{\Omega_k} \left(\mathbf{N}^\intercal \left(\nabla \mathbf{N}\right)_i + \tau_{\mathrm{PSPG}} \left(\nabla \mathbf{N}\right)_i^\intercal \mathbf{u}_{\mathrm{adv}} \nabla \mathbf{N} \right) \mathrm{d}\Omega_k \tag{8}$$

$$A_{pp} = \int_{\Omega_k} \tau_{\mathrm{PSPG}} \frac{1}{\rho} \nabla \mathbf{N}^\intercal \nabla \mathbf{N} \mathrm{d}\Omega_k \tag{9}$$

$$A_{u_i u_i} = \int_{\Omega_k} \left(\nu \nabla \mathbf{N}^\intercal \nabla \mathbf{N} + \left(\mathbf{N} + \tau_{\mathrm{SUPG}} \mathbf{u}_{\mathrm{adv}} \nabla \mathbf{N}\right)^\intercal \mathbf{u}_{\mathrm{adv}} \nabla \mathbf{N} + \tau_{\mathrm{BULK}} \left(\nabla \mathbf{N}\right)_i^\intercal \nabla \mathbf{N}_i \right) \mathrm{d}\Omega_k \tag{10}$$

$$A_{u_i u_j} = \int_{\Omega_k} \tau_{\mathrm{BULK}} \left(\nabla \mathbf{N}\right)_i^\intercal \nabla \mathbf{N}_j \mathrm{d}\Omega_k \qquad (i \neq j) \tag{11}$$

$$A_{u_i p} = \int_{\Omega_k} \frac{1}{\rho} \left(\mathbf{N} + \tau_{\text{SUPG}} \mathbf{u}_{\text{adv}} \nabla \mathbf{N}\right)^{\intercal} (\nabla \mathbf{N})_i \, \mathrm{d}\Omega_k \tag{12}$$

$$T_{p u_i} = \int_{\Omega_k} \tau_{\text{PSPG}} \, (\nabla \mathbf{N})_i^{\intercal} \, \mathbf{N} \mathrm{d}\Omega_k \tag{13}$$

$$T_{u_i u_i} = \int_{\Omega_k} \left(\mathbf{N} + \tau_{\text{SUPG}} \mathbf{u}_{\text{adv}} \nabla \mathbf{N}\right)^{\intercal} \mathbf{N} \mathrm{d}\Omega_k \tag{14}$$

In these equations, the indices i and j refer to the i-th or j-th row of the gradient matrices of the shape functions and thus take values 0, 1 and 2 for three-dimensional problems. We note that the advective and SUPG terms contain an advection velocity $\mathbf{u}_{\text{adv}}$, which is introduced to obtain a linear system. The value of $\mathbf{u}_{\text{adv}}$ is obtained through a series expansion as detailed by [3].

In order to obtain the final discrete system, equation (5) is transformed, introducing a θ-method for the time discretization and solving for the difference $\Delta \mathbf{x}_e = \mathbf{x}_e^{n+1} - \mathbf{x}_e^n$ between two subsequent time steps::

$$\left(\frac{1}{\Delta t} T_e + \theta A_e\right) \Delta \mathbf{x}_e = -A_e \mathbf{x}_e^n \tag{15}$$

Setting $\theta = 1$ yields a backward Euler method, while setting $\theta = 0.5$ results in the second order accurate Crank-Nicolson scheme. We note that some flexibility in this choice is useful, since even though both methods are unconditionally stable in theory, numerical simulations show that some instability in the pressure solution may appear during the first time steps if the Crank-Nicolson scheme is applied from the start.

Finally, the element contributions need to be summed together over the domain, resulting in a global linear system. Because the shape functions $\mathbf{N}$ are defined locally, the system is sparse and can be solved using iterative techniques such as GMRES.

2.2. Implementation

The implementation is usually accomplished by writing out the element matrices A_e and T_e for each element type that needs to be considered, and then calling an assembly procedure. Due to the complexity of the code, the link with the mathematical formulation is lost, and adding support for new element types requires a lot of repetitive work. The method proposed here alleviates these concerns, by providing a higher level of abstraction that closely resembles the expressions (8) to (14).

Using the Boost Proto library [7], we implemented a "Domain Specific Embedded Language" (DSEL) for the construction of FEM discretizations. The use of C++ template metaprogramming techniques allows for a high level of abstraction with a minimal loss in runtime performance. Because the language is embedded, it just compiles along with the rest of the C++ code, without any need for external preprocessing. Let's introduce the DSEL by looking at the first contribution to the element matrix, A_{pu_i} from equation (8). It is written in code as:

```
1 _A(p, u[_i]) += transpose(N(p)) * nabla(u)[_i] +
2   c.tau_ps*transpose(nabla(p)[_i])*u_adv*nabla(u)
```

The resemblance with equation (8) is immediately obvious. In the above expression, p and u are variables that have been defined to be associated with a scalar and vector field, using the following declarations:

```
1 MeshTerm<0, VectorField> u("Velocity", Tags::
      solution());
2 MeshTerm<1, ScalarField> p("Pressure", Tags::
      solution());
```

These declarations indicate that u and p are so-called Proto terminals, which means that by deriving from a Boost Proto class, they have a full set of Proto overloads. The 0 and 1 in the declarations are needed to make sure that each variable can be identified at compile time. Likewise, the operations such as transpose and nabla that appear in the expressions are also terminals, but they have been predefined in the Coolfluid 3 framework. The `nabla` terminal represents $\nabla \mathbf{N}$, but in the code it takes a variable as a parameter, to allow for different shape functions for each variable. The appearance of the predefined index `_i` indicates that a loop over the number of physical dimensions should be made.

When applying operators to the terminals (plus-assign, function call, product, ...) the result is an expression tree object that is then executed in a loop over the mesh. In order to evaluate the expression, a data object is passed along to the evaluation function to give access to the nodal values and the geometric mesh data. Because the whole system relies on template meta programming, the data that is passed can use fixed-size matrix and vector types, which allows for better code optimization at compile time.

In order to apply the integration over the element, a second-order Gauss quadrature is applied. It is inserted into the expression tree by calling the function `element_quadrature`. The full code for the assembly procedure is shown in listing 1. Note that here we start by defining a list of admissible element types. By executing a Boost MPL loop, code for each of these element types is generated, and the selection of which code to use is automatically made at runtime, based on the type of mesh that is used. This also easily en-

ables the use of heterogeneous meshes that combine triangles and quadrilaterals, for example.

Care needs to be taken when calculating the values of the stabilization coefficients, and we use a procedure that calculates a unique value for each element, based on the local Reynolds number. Such special needs can be handled by implementing a user-defined function, ready for use inside an expression. Here, we have defined `compute_tau`, which is simply declared as:

```
struct ComputeTau
{
  typedef void result_type;

  template<typename UT>
  void operator()(const UT& u, SUPGCoeffs& c) const
  {
    // do calculation here
  }
};
static MakeSFOp<ComputeTau>::type const compute_tau
    = {};
```

All that is needed is a struct with a function call operator, templated by the variables that are used. In this case, `UT` represents the data associated with the velocity field, and it can be used to access the underlying geometry, the current values and gradients. The `SUPGCoeffs` class is simply a struct that holds the different coefficients as well as the density and viscosity. The implementation allows defining custom functions with any number of parameters of any type. The return type is specified using the "result of" protocol, which here reduces to a simple typedef. The user defined function is made available for use in expressions by constructing a `compute_tau` terminal.

Finally, the assembly is written using the + = operator for the system matrix and right hand side.

```
elements_expression
(
 boost::mpl::vector4<LagrangeP1::Triag2D,
      LagrangeP1::Quad2D, LagrangeP1::Tetra3D,
      LagrangeP1::Hexa3D>(),
 group
 (
  _A = _0, _T = _0,
  compute_tau(u, c),
  element_quadrature
  (
   _A(p, u[_i]) += transpose(N(p)) * nabla(u)[_i] +
        c.tau_ps * transpose(nabla(p)[_i]) * u_adv
       *nabla(u),
   _A(p, p) += c.tau_ps * transpose(nabla(p)) *
       nabla(p) * c.one_over_rho,
   _A(u[_i], u[_i]) += c.mu * transpose(nabla(u)) *
        nabla(u) * c.one_over_rho + transpose(N(u)
        + c.tau_su*u_adv*nabla(u)) * u_adv*nabla(u
       ),
   _A(u[_i], p) += c.one_over_rho * transpose(N(u)
       + c.tau_su*u_adv*nabla(u)) * nabla(p)[_i],
   _A(u[_i], u[_j]) += c.tau_bulk * transpose(nabla
       (u)[_i]) * nabla(u)[_j],
   _T(p , u[_i]) += c.tau_ps * transpose(nabla(p)[
       _i]) * N(u),
   _T(u[_i], u[_i]) += transpose(N(u) + c.tau_su*
       u_adv*nabla(u)) * N(u)
  ),
  system_matrix += invdt() * _T + _A,
  system_rhs += -_A * _x
 )
);
```

Listing 1: Matrix assembly

2.3. Validation

A first validation was performed on a 2D backward facing step. This problem was chosen because of its simple geometry and boundary conditions, and because of the abundance of reference data in the literature. We compared with experimental data from [8] up to a Reynolds number of 400. Meshing guidelines were obtained from a previous numerical study by [9]. Figure 1 shows good agreement with the measured data. At Reynolds numbers above 400, the flow becomes three dimensional. The case of Re = 648 was considered, resulting in a normalized reattachment length of 10.28, showing again excellent agreement with [8] and [9]. Performance for the 3D case was not satisfactory, due to the long solution times required for the linear system. An improved preconditioning of the linear system should go a long way towards improving the performance and scalability of the solver. The methods proposed in [10] and [11] seem very appropriate for our discretization scheme, and promise a substantial performance increase.

3. Experimental setup

A first experiment that is being developed is designed to measure concentration variations and the effect of particle coagulation in a flow field that should be reproducible using numerical simulation. Flow enters a cubic chamber through a narrow slot near the bottom, and exits near the top of the opposite wall (see Fig. 2). For the particle coagulation, a short burst of particles will be injected near the center of the circulation zone.

In order to get a reproducible result, the inlet conditions are controlled using a device similar to the inlet section of a subsonic wind tunnel, as shown in Fig. 3

3.1. First measurement results

To get a first look at the flow field, PIV measurements at the vertical center plane in the length-wise direction were made. Figure 4 shows the velocity vectors, confirming the existence of the circulation zone.

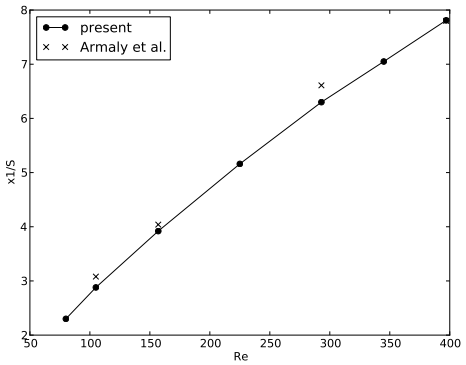

Figure 1: Normalized backward facing step reattachment length as a function of Reynolds number.

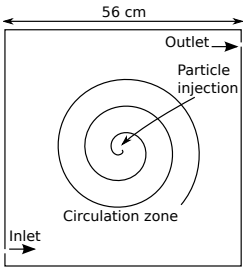

Figure 2: Schematic of the experimental test chamber.

Figure 5 shows the evolution of the X-velocity along the vertical center line for different fan settings indicated on the fan controller. As expected, the strength of the recirculation increases proportionally to the fan power. It should be noted that these are only preliminary results and an error analysis using synthetic images still needs to be performed, so for now the results are presented without any error indication. During the measurements, some practical problems were encountered with regard to the seeding of the flow. A Laskin tube was used to seed the flow with olive oil droplets at the inlet of the fan, on the left in figure 3. For any attainable particle flow, however, the test chamber was quickly filled with particles, resulting in a density far too high to correlate the PIV images. The problem was solved by turning off the seeding flow before the measurements, and take measurements while the box

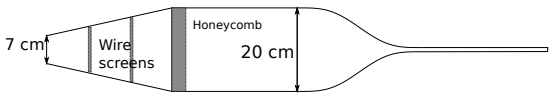

Figure 3: Conditioning of the test chamber inlet.

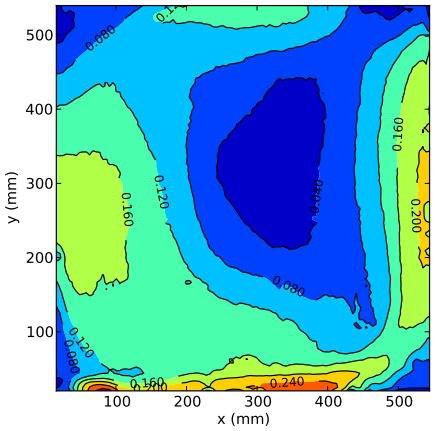

Figure 4: Contours of velocity magnitude, for a fan setting of 10.

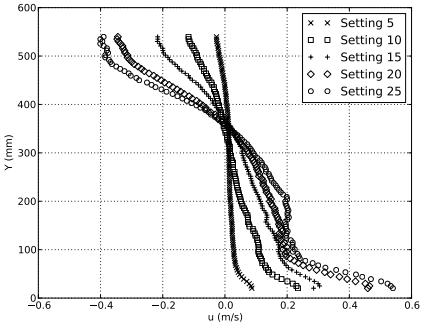

Figure 5: Evolution of the X-velocity along the vertical center line

was being cleared of particles. During these experiments, it was clear that a higher density of particles remained near the center of the box for long durations, exceeding 200s at fan setting 10. This observation is encouraging for the later particle coagulation experiments.

4. Conclusion and future work

The objective of the current work is to provide a meaningful contribution to the numerical modeling of dispersed phase flow. The inclusion of nanoparticles and coagulation effects constitute new challenges, and should extend the applicability of the method. Areas of application include for example indoor air quality or risk assessment when considering the behavior of chemical or biological agents, as well as the study of

pollutant aggregation in close proximity to the source.

Current work will be continued by extending the current flow solver with LES for turbulence modeling, which will be tested against the PIV data as well as channel DNS from i.e [12]. Once the flow field is validated, particle and coagulation modeling will be introduced, with validation against literature data, i.e. [13; 14; 15] as well as PDA measurements in the current test chamber.

Acknowledgements

The current implementation of the Navier-Stokes solver was realized thanks to the valuable assistance and comments of Tamás Bányai. For the PIV setup, the assistance from Elmar Recker was greatly appreciated.

References

[1] C. A. Pope, D. W. Dockery, Health Effects of Fine Particulate Air Pollution: Lines that Connect, J. Air & Waste Manage. Assoc. 56 (2006) 709–742.

[2] G. Oberdörster, E. Oberdörster, J. Oberdörster, Nanotoxicology: An Emerging Discipline Evolving from Studies of Ultrafine Particles, Environ Health Perspect 113 (2005) 823–839. doi:10.1289/ehp.7339.

[3] T. Bányai, D. Vanden Abeele, H. Deconinck, A fast fully-coupled solution algorithm for the unsteady incompressible Navier-Stokes equations, in: Conference on Modelling Fluid Flow (CMFF'06), Budapest, Hungary, 2006.

[4] M. S. Alnæs, K.-A. Mardal, On the efficiency of symbolic computations combined with code generation for finite element methods, ACM Transactions on Mathematical Software 37 (1) (2010) 1. doi:10.1145/1644001.1644007.

[5] C. Prud'homme, Life: Overview of a Unified C++ Implementation of the Finite and Spectral Element Methods in 1D, 2D and 3D 4699 (2007) 712.

[6] H. G. Weller, A tensorial approach to computational continuum mechanics using object-oriented techniques, Computers in Physics 12 (6) (1998) 620. doi:10.1063/1.168744.

[7] E. Niebler, Proto: a compiler construction toolkit for DSELs, in: Proceedings of the 2007 Symposium on Library-Centric Software Design - LCSD '07, LCSD '07, ACM, New York, NY, USA, 2007, pp. 42–51.

[8] B. F. Armaly, F. Durst, J. C. F. Pereira, B. Schönung, Experimental and theoretical investigation of backward-facing step flow, Journal of Fluid Mechanics 127 ( ) (1983) 473–496. doi:10.1017/S0022112083002839.

[9] P. T. Williams, A. J. Baker, Numerical simulations of laminar flow over a 3D backward-facing step, International Journal for Numerical Methods in Fluids 24 (11) (1997) 1159–1183.

[10] M. Benzi, M. A. Olshanskii, Z. Wang, Modified augmented Lagrangian preconditioners for the incompressible Navier-Stokes equations, International Journal for Numerical Methods in Fluids (2010) n/adoi:10.1002/fld.2267.

[11] T. Heister, G. Rapin, Efficient augmented Lagrangian-type preconditioning for the Oseen problem using Grad-Div stabilization, International Journal for Numerical Methods in Fluidsdoi:10.1002/fld.3654.
URL http://dx.doi.org/10.1002/fld.3654

[12] R. D. Moser, J. Kim, N. N. Mansour, Direct numerical simulation of turbulent channel flow up to $Re_\tau = 590$, Physics of Fluids 11 (4) (1999) 943–945. doi:10.1063/1.869966.

[13] M. Chen, K. Kontomaris, J. B. McLaughlin, Direct Numerical Simulation of Droplet Collisions in a Turbulent Channel Flow. Part II: collision rates, International Journal of Multiphase Flow 24 (November 1999) 1105–1138.

[14] J. R. Fessler, J. D. Kulick, J. K. Eaton, Preferential concentration of heavy particles in a turbulent channel flow, Physics of Fluids 6 (11) (1994) 3742. doi:10.1063/1.868445.

[15] M. Sommerfeld, Analysis of collision effects for turbulent gas-particle flow in a horizontal channel. Part II. Integral properties and validation, International Journal of Multiphase Flow 29 (4) (2003) 701. doi:10.1016/S0301-9322(03)00033-8.

Flow visualization and Planar Laser Induced Fluorescence (PLIF) measurements on horizontal shear-driven liquid films at the edge of a plate[☆]

Evangelos Bacharoudis[*]

Univ. Lille Nord de France, France, bacharoudis@vki.ac.be

Supervisor: Jean-Marie Buchlin

Professor, Head, Environmental and Applied Fluid Dynamics Department, von Karman Institute for Fluid Dynamics, Belgium, buchlin@vki.ac.be

University Supervisor: Larbi Labraga

Professor, Univ. Lille Nord de France, France, larbi.labraga@univ-valenciennes.fr

Industrial Partner: Hervé Bratec

Dr. Engineer, Robert Bosch Produktie N.V., Belgium, herve.bratec@be.bosch.com

Abstract

In this study a shear-driven liquid film on a horizontal plate of low surface energy approaching a sharp corner is investigated experimentally by means of high speed recording and Planar Laser Induced Fluorescence (PLIF). The liquid film is free to expand towards the spanwise direction of the test section. Different atomization regimes have been recognized and a map is proposed. The behavior of the liquid film under various flow conditions including the critical ones for the onset of separation is described. An empirical equation is given in order to define the onset of liquid film atomization.

Keywords: shear-driven film, PLIF, wave velocity, film thickness, critical conditions

1. Introduction

Liquid films driven by an external air flow are encountered very often in the industrial and natural environment. These films can flow over solid surfaces and depending on both the flow conditions and the geometry of the solid surface can be detached and atomized in small droplets. In the industrial domain, the generation of small droplets which usually follow the flow of the external air, can lead to either desirable or detrimental effects for the engineering applications. In all the cases, knowledge of the behavior of the liquid film in different flow conditions is necessary in order to predict the onset of these atomization phenomena and minimize or maximize their effects. On the other hand, optimization of the engineering applications can be accomplished from the understanding of the physics behind the liquid film and air flow interactions. A short review concerning mainly the experimental studies of shear-driven liquid films and their separation due to geometrical changes of the solid surfaces is given below.

Shear-driven films have been studied extensively for decades mainly in two configurations, the circular pipes and the rectangular channels. There is a vast bibliography concerning the study of liquid films encountered in annular flows dating back from the early experiments of Wallis and other researchers [1, 2, 3] to the more contemporary studies [4, 5, 6, 7]. Vertical, inclined and horizontal configurations have been used in combination with co-current and counter-current air-liquid mixtures in different flow conditions. In these studies the charac-

[*] Corresponding author

teristics of the mean shear-driven liquid film and the wavy interface have been measured in order to learn more about the mechanism of momentum, mass and heat transfer in annular flows and develop models able to predict the air-liquid interaction and specifically the interfacial shear.

Less in number studies have been conducted in rectangular channels. Jurman and McCready [8] studied experimentally the waves on a shear-driven liquid film and combined the measurements with predictions from the stability analysis. Wittig et al. [9] measured the thickness and wave velocity of a thin film on a flat plate inside a rectangular test section. The facility represents the configuration of a simplified prefilming air-blast atomizer. They showed that the laminar velocity profile fits better their experimental results for the liquid film flow. The investigation of the local characteristics of the liquid films in horizontal and vertical channels has been carried out by Kang and Kim [10] in order to develop a model for describing the interfacial shear stress. Recently, Friedrich et al. and Lan et al. [11, 12] measured and simulated with CFD the thickness and width of a shear-driven liquid film in rectangular channel which is free to expand in a spanwise direction. Finally, Lorencez et al. [13] investigated the local turbulent structures emerged from the air-liquid interaction on a stratified flow. It is one of the very few works on stratified flows conducted in open channel with relatively thin liquid media.

In all the above studies several experimental methods have been utilized in order to measure the liquid film thickness and extract useful information for the interface. Briefly, the capacity method, the conductivity method, the light absorption technique, the shadow method, the fluorescence method, the interferometric method are some of the methods used for the investigation of the shear-driven liquid films. The studies revealed that waves emerge on the interface due to the air-liquid interaction and become three dimensional very fast, especially, in higher air velocities. Concerning the characteristics of the liquid film, generally, the film thickness is increased with the liquid flow rate and is reduced with the increase of the air velocity. On the other hand, both, the liquid flow rate and the air flow above the film result in the increase of the wave velocity. Finally, when the liquid film is not restricted at its sides by the walls of the circular or rectangular channels, the film width seems to increase with the liquid flow rate and the air velocity.

The shear-driven liquid films when encounter a change in the geometry flowing above may separate from the wall surface depending on the flow conditions and the geometrical characteristics, resulting in the primary atomization of the liquid film into droplets. Very few studies have been conducted in order to determine the critical conditions in which the onset of the detachment and the primary atomization is taking place and even less to obtain sufficient experimental results in this limit. One of the early theoretical works on the liquid film detachment flowing over a smooth bent is the one of Owen and Ryley [14]. They presented many different factors that can affect the liquid film flow around the bent. They confirmed that the surface tension is the necessary force in order to hold the film on to the boundary wall, the inertia or centrifugal forces of the film cause the detachment from the wall and the gravitational forces may act either as adhesive forces or as repelling ones. They tried to support their analysis with few experiments, however their experimental results were very poor. Azzopardi and Sanaullah [15] have investigated the film separation in wave-plate mist eliminators. A model for the prediction of the critical conditions has been proposed based on the model of [14]. They supported their model with a number of experiments conducted by themselves and by collecting experimental data from other researchers in literature. A theoretical model for the determination of the critical conditions leading to liquid film detachment based on stability analysis has been developed by Maroteaux et al. [16]. According to their study the main reason for film separation is Rayleigh-Taylor instabilities growing when the film turns around a corner. They provided few experimental results using the PLIF method to verify their model. Finally, Firedrich et al. [17] and Wegener et al. [18] proposed a criterion for the onset of separation of shear driven films based on force balance as a function of local parameters of the flow. Their model is supported by a significant number of experimental results. However, they report that the experimental method for measuring the atomized mass is inaccurate close to the critical conditions and conclude that the identification of the critical conditions is an arbitrary process. Scrutinizing the literature, more detailed experiments are needed in order to understand the process of film detachment and determine the critical conditions for the onset of the atomization.

In this study a horizontal liquid film, free to expand towards the spanwise direction is sheared by a turbulent wall jet developed on the flat plate of an open channel. The liquid film is driven towards a sharp corner at the edge of the plate. Initially, the characteristics of this type of liquid film flow have been investigated using high speed recording in order to

gain understanding of the behavior of the film on the plate. Next, detailed measurements of the film thickness, width and velocity have been carried out with the PLIF method in order to identify the critical conditions for the onset of the film atomization. An empirical model is proposed from the experimental results.

2. Test facility and methods

The test facility used in this project in order to study the behavior of the shear-driven liquid film and its atomization in a sharp corner is presented in Figure 1. It is consisted mainly on three parts the wind tunnel, the hydraulic circuit and the test section.

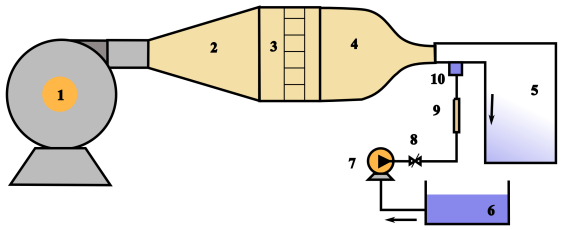

1. FAN
2. DIFUSSER
3. SETTLING CHAMBER
4. CONTRACTION
5. TEST SECTION
6. RESERVOIR
7. PUMP
8. BALL VALVE
9. ROTAMETER
10. CONTAINER

Figure 1: Experimental facility for the study of the shear-driven liquid film on a horizontal plate near a sharp corner.

An open circuit, blowing type, low speed wind tunnel has been manufactured in order to support different test section configurations. The wind tunnel is consisted of the fan of 11 kW, the diffuser, the settling chamber and the contraction. Special care has been given to the design of the 2D contraction in order to have an air flow of acceptable quality with minimum variations of the mean flow. The contraction ratio achieved at the design is 10.

The hydraulic circuit is mounted at the bottom of the test section and recirculates distilled water from the reservoir to the horizontal plate. A small container is fixed below the horizontal plate of the test section in order to collect the liquid and cut down significant disturbances generated by the system. The liquid enters the test section through a rectangular slit of spanwise length of 100 mm and opening of 1mm. The flow rate of the liquid introduced in the test section is measured by means of a rotameter with ±2 l/h uncertainty.

The test section is consisted of two plates one horizontal and one vertical comprising a sharp corner of 90°. The two plates made by Polycarbonate are restricted by two side walls from PMMA forming a short open channel. The side walls are used in order to avoid disturbances from the environment, especially at the region where liquid phase detachment occurs. The whole test section is transparent in order to apply different optical methods for the liquid film study. The test facility has been placed in a large room in order to avoid perturbations from the jet flow developing at the exit of the wind tunnel.

A detailed flow visualization study has been conducted using high speed recording. A side camera view with a backward light configuration has been realized in order to study the shear-driven film and its wavy interface on the plate while a top view with a front light setup has been utilized for the investigation of the liquid film atomization at the corner. The high speed camera works at 1000 fps for all the cases. Information concerning the wave velocity of the liquid film interface are extracted from the side view of the high speed recordings. A program based on the image analysis toolbox of Matlab has been developed in order to detect the interface from the shadow images and calculate the wave velocity cross-correlating the signal of the film thickness in two fixed positions of distance of 5 mm on the film. Though the film thickness is not calculated correctly due to the fact that all the waves which belong to the foreground or the background are projected as a shadow on the plane of the camera, however, their velocity is believed to be calculated with reasonable accuracy. The motion of the waves is independent on the precise calculation of their height. It depends on the distance of the two probes and the time needed for them to travel between the two probes. The overall uncertainty of the wave velocity calculation is estimated at ±0.05 m/s for low wave velocities and ±0.31 m/s for the maximum ones.

Planar Laser Induced Fluorescence (PLIF) has been used in order to detect the interface and extract the film thickness. Figure 2 shows the plane of measurements of the PLIF setup. Data have been measured at the edge of the corner in order to correlate them with the atomization occurring in that region especially for the critical conditions. With the PLIF method the liquid film is visualized and the resulting images are post processed with a Matlab program based on the interface detection through intensity variations. Fluorescein with maximum absorption wavelength at 490 nm and maximum emission wavelength at 518 nm is added in the reservoir as a fluorescent dye in a concentration of 100 mg/l. An Nd:YaG, green (532 nm), single pulse laser illumi-

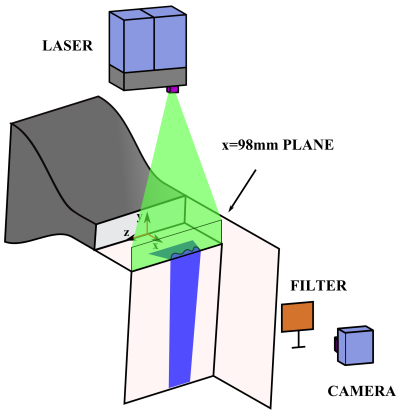

Figure 2: PLIF setup and film thickness plane of measurements.

nates the cross section of the film at the corner with a frequency of 7 Hz. The camera equipped with a lens of 105 mm captures a window of 145 mm length of the liquid film. A filter is used to suppress the laser light. The images collected are statistically independent and the average film thickness is calculated from the interface detection with a maximum overall uncertainty of ±0.21 mm.

Mass measurements have been carried out for the identification of the critical conditions. When the liquid film stops to be atomized at the sharp corner and no droplets are generated, the critical conditions have been captured. The atomized mass is collected with a small flat plate positioned downstream the corner in a distance of 5 mm from the vertical wall of the test section. From the high speed recording when the facility works close to the critical conditions the generated droplets possess enough inertia in order to be detached from the wall but at the same time their inertia is low in order to let them escape from the test section. Thus, all the droplets are collected in the plate and are weighed by means of a digital balance with overall uncertainty of ±0.01 gr. The method becomes inaccurate and stops working for high air velocities. Apart from the mass, the width of the film has been measured by placing a ruler below the transparent test section and taking pictures with a SLR digital camera from the top. The uncertainty of method is estimated at ±1 mm. From the measured magnitudes of the liquid film flow rate, the film thickness and the width, the mean film velocity has been calculated at the corner cross section with an overall maximum uncertainty of ±0.01 m/s.

3. Flow visualization

3.1. Atomization regimes

A liquid film on the order of 1-2 mm is formed on the horizontal polycarbonate surface of the test section. The critical surface energy of the polycarbonate surface is 30 mN/m and the working liquid is distilled water. The wetting of the solid surface from the working liquid is 'partial' according to Zisman's criterion [19] since the surface tension of water is quite higher than the critical energy of the surface. For this liquid-solid combination a detailed flow visualization study has been carried out and different atomization regimes have been identified. Figure 3 presents the atomization map that is proposed in order to describe the way a horizontal shear-driven liquid film is atomized at the edge of a low energy wall surface. The atomization regimes are expressed as a function of the air velocity and the liquid film Reynolds number which is based on the flow rate and the length of the slit.

Different patterns are formed on the free interface of the shear-driven liquid film and different ways of atomization are depicted by the film after the corner depending on the flow conditions. First, the atomization map can be separated in two parts, the part where there is no atomization and is located at the left of the critical curve and the part of the atomization which is at the right. The last part can be divided in regions and each region corresponds to a certain way of liquid film atomization at the sharp corner.

In Figure 3, region I is the area close to the critical conditions where low to moderate atomization occurs. A liquid film in that regime depicts regular 3D disturbances on its interface which evolute into ligaments at the corner traveling downwards on the vertical wall. Droplets are generated from these ligaments. The regime is encountered for either low air velocities or low film Reynolds numbers.

Increasing the speed of the air flow and the film Reynolds number the atomization regime of the region II occurs. In that regime the free interface of the film is dominated by 3D waves forming a kind of 'cellular' pattern. The atomization mass increases to moderate rates. The waves of the interface form ligaments when encounter the corner and break towards the streamwise direction into droplets due to the strong air flow. The bursts of these ligaments occur along a large part of the spanwise direction of the film. A transition zone exists between the regions I and II where both atomization regimes appear on the film simultaneously.

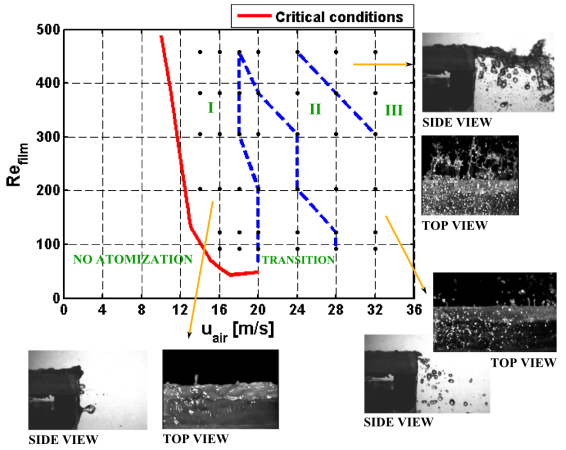

Figure 3: Atomization map for the horizontal shear-driven liquid film.

For the higher air velocities and liquid flow rates tested in this work a third regime is encountered in region III. The external shear is high enough in order to drift the liquid film downstream the corner and form a liquid sheet. The liquid sheet is divided in small cells which evolute into ligaments which break at the direction of the flow. This pattern is similar to the one identified in the studies on the prefilming atomizers [20] for high air and low liquid velocities. The free interface presents the same structure as in the region II with 3D waves of shorter wavelength. The atomization rate is very high.

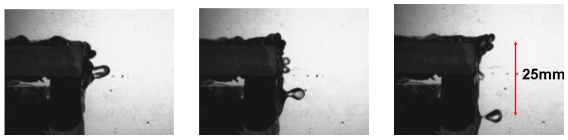

(a) t=0 sec (b) t=0.4 sec (c) t=1.2 sec

Figure 4: Different time instants for the droplet detachment from the film. The flow conditions belong to the region I

It is interesting to examine better the droplet generation in conditions very close to the critical ones shown in Figure 4. Three different instants of droplet detachment from the bulk of the film are presented. The ligament which is formed at the corner is deformed as it is moving downwards and develops a head. When this head grows enough a droplet is generated from the break-up of the ligament. In other cases, if the ligament is long enough, it can break in several droplets as it falls down. In all the cases the ligament break-up takes place quite far from the region of the corner. Another interesting point is the fact that the ligaments which produce droplets emerge sporadically and in an irregular manner along the width of the film. Summarizing, at the critical conditions, the onset of atomization of a horizontal, sher-driven liquid film is accompanied by the formation of few sporadic ligaments which break into droplets traveling downwards on the vertical wall. Neither detached film along the spanwise direction like a liquid sheet appear in these conditions nor spanwise ligaments occur.

3.2. Wave velocity

The images from the flow visualization with the back light configuration have been used in order to calculate the velocity of the waves traveling along the test section. Close to the critical conditions the calculation is not possible due to the limited number of disturbances on the interface. Figure 5 presents the wave velocity for different air velocity and liquid film Reynolds number (based on the flow rate and the width of the slit). The same trend is observed as reported in literature for this horizontal shear-driven film. Increasing the liquid Reynolds or the external shear the waves on the interface seem to accelerate. Direct comparison with data from the literature is not achieved due to the different range of flow conditions among this study and the other works in the literature and the different way the film is formed on the flat plate. In this study, the film is sheared by a turbulent jet and is free to expand towards the spanwise direction.

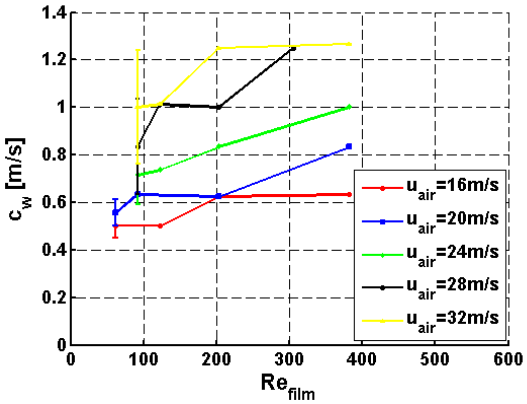

Figure 5: Wave velocity as a function of the Re_{film} and the air velocity.

4. PLIF measurements

4.1. Liquid film characteristics in region I

A liquid film can obtain different forms when it flows over a horizontal plate without restriction in expanding towards the spanwise direction. Consequently, the behavior of the liquid film and the primary atomization will change for every different film formation. The final form of the film on the plate depends on the initial conditions, the boundary conditions and the ambient conditions of the experiment. In this study, a considerable effort has been made in order to keep all the conditions constants or at least to minimize their variation. However, the ambient conditions, especially the temperature of the air and film flow, will vary in a short range of values due to the design of the experimental facility and the initial conditions, mainly due to the operation of the pump for the film formation will also slightly change among the tested cases. The results presented below represent this effort to maintain the conditions of the experiment invariable.

The liquid film characteristics of the shear-driven film developed on the horizontal plate are depicted in Figure 6 as a function of the air velocity and the liquid Reynolds number (based on the flow rate and the length of the slit). First, the efficiency of the liquid film in primary atomization is evaluated by measuring the atomized mass. In Figure 6a, the percentage of the total mass which is atomized at the sharp corner is presented. As expected, an increase of the liquid Reynolds number or the air velocity enhances the atomization.

The mean film velocity at the corner section is calculated from the measurements of the thickness, width and total flow rate of the liquid film at the same section. Raising both the inertia of the film or the external shear on the interface, Figure 6b, the mean film velocity increases.

The area of the liquid film cross section at the corner has been calculated from the film width and thickness as shown in Figure 6c. An increase of the external shear results in smaller cross sections which implies that the film is compressed. On the other hand, an increase of the film inertia is accompanied by an augmentation of the cross section area. The opposite trend is observed for the film sheared by the air velocity of 13 m/s. It has to do with the uncertainties of the film formation on the plate which is only partially controlled. The resulted film shows a steeper slope on the reduction of the thickness when the film inertia increases.

Figures 6d and 6e present the measurements of the film width and thickness at the edge of the corner. Concerning the width, raising the air velocity and the liquid Reynolds number the film is expanding on the flat plate towards the spanwise direction. Conversely, increasing the speed of the air and the liquid film flow results in films with lower thickness. The last shows that the behavior of the horizontal shear-driven liquid film depends on the wetting effects of the surface since the latter can determine how widely the liquid film is spread on the flat plate and consequently what will be the influence on the final film thickness and width.

Finally, Figure 6f presents the percentage of the root mean square of the film thickness comparing it to the value of the film thickness. This magnitude can be considered as a mean to measure the fluctuations emerging on the free interface of the film. Though there is a lot of uncertainty, it could be inferred that the fluctuations of the film grow with increasing liquid Reynolds. On the other hand, it is not clear what is happening with the increase of the air velocity, though, a trend of raising the RMS of the film thickness is observed fot higher velocities.

The results presented above signify a different tendency on the liquid film behavior comparing to the one reported in literature. Although there are no results for horizontal films, free to expand in any direction and flowing inside an open channel, there are many experimental data for annular flows [5, 6, 7] and flows inside rectangular ducts [9, 12]. In annular flows the shear-driven liquid film reduces its thickness with increasing shear, like it is reported here. However, the increase of the liquid Reynords number results in the development of the film thickness at the bottom wall of the circular pipes in contrast to what is mentioned in this study. This is explained by the fact that the liquid film generated in this work is expanding faster at the spanwise direction than the normal one resulting in wider liquid films with less thickness. The films inside the circular pipes have to overcome the action of gravity in order to expand towards their circumferential direction.

Inside the rectangular channels where the liquid film is expanding from one side of the channel to the other, the same trend is observed as for the annular flows. Again the same arguments are provided in order to explain the difference of the film behavior. It is interesting to notice that the experimental results presented from Lan et al. [12] concerning the film width and thickness for a shear-driven film without side restrictions in a channel agree well with the behavior of the film described here. In their study, in some cases

the film thickness is reduced with increasing liquid flow rate. Nevertheless, they do not explain the differences in the trend on the film thickness observed in their study, probably due to the high uncertainty of the measurement or the limited number of experimental evidence which would permit the drawing of a safe conclusion. They deduce conclusions similar to the one reported in the studies for the annular flows or the flows inside channels.

4.2. Critical conditions

The local characteristics of the horizontal shear-driven liquid film for the critical conditions have been investigated from the PLIF measurements. Before discussing the results, the term critical conditions has to be clarified and the way used to capture these conditions has to be presented.

The critical conditions have been determined by collecting and weighing the atomized mass ejected from the sharp corner, as mentioned in section 2. Figure 7 presents typical diagrams of mass measurements carried out in this study. The air velocity is fixed in a constant value and the inertia of the film is reduced by changing the flow rate of the liquid film. A total number of 20 acquisitions has been conducted and each acquisition has a duration of 2 min for every tested case.

In Figures 7a-7d the atomized mass collected after the corner is decreased with the liquid Reynolds number. For relatively high liquid Reynolds 7a, there is a significant amount of atomized mass captured downstream the corner. For lower liquid Reynolds first the atomized mass seem to be independent of the acquisition, Figure 7b. Then, the collection of the atomized mass is becoming irregular and intermittent until a minimum liquid film Reynolds below of which there is no atomization. Critical conditions are the flow conditions expressed as the pair of $We_{aerodynamic}$ and Re_{film} which cause a negligible amount of the mass of the film to be atomized at the corner. The limit for the negligible amount of atomized mass is when the latter start to become independent on the acquisition. This amount of mass is always less than the 0.05% of the total mass introduced inside the test section of the facility. For the case presented in Figure 7, any tested case which produce diagrams like presenting in Figures 7c and 7d would be consider as critical. Thus, the critical conditions are expected to obtain the form of a cloud in a diagram with axes the pair of the non-dimensional numbers of liquid Reynolds and Weber number.

The behavior of the local parameters of the shear-driven liquid film have been investigated extensively under critical conditions. After the pair of flow magnitudes is identified as critical, detailed measurements with the aid of the PLIF method are carried out in order to determine the liquid film thickness, width, mean velocity and RMS on these critical conditions. Experimental results for different critical conditions are presented in Figure 8.

The mean critical film velocity at the corner is calculated from the measured values of the liquid film thickness, width and flow rate. Increasing the external shear, the mean velocity of the film has to be decreased in order the liquid film to remain attached on the wall at the edge of the corner without being atomized. The trend of the mean critical film velocity is shown in Figure 8a.

It is important to notice that increase of the air velocity in the diagrams of Figure 8 signifies simultaneous reduction of the liquid flow rate in order to maintain the liquid film under critical conditions. Thus, the tendency of the critical film width, shown in Figure 8b, is to become more narrow with increasing air velocity since at the same time the liquid flow rate has been reduced.

Concerning the critical mean film thickness at the edge of the flat plate, generally, it is decreased when the shear on the liquid film is increased, Figure 8c. However, for low values of external shear, an opposite trend is observed. The liquid film thickness is decreasing with decreased shear. This is explained by the fact that as the external air velocity reduces the liquid flow rate is increased in order to keep the critical conditions resulting in a liquid film which develops towards the normal direction. However, after a certain amount of liquid film mass inserted inside the test section, the film seems to become heavy enough and the contact line at the sides of the film incapable to support the heavy film. The latter results in the spreading of the film towards the spanwise direction on the horizontal plate and thus triggering the reduction of the critical film thickness.

The percentage of the critical root mean square of the film thickness comparing it to the critical mean film thickness is depicted in Figure 8d. This ratio could be interpreted as a mean which records the fluctuations occurring on the interface of the film. Despite the large scattering of the experimental data which obscure the drawing of safe conclusions, a tendency can be recognized. It seems that for a liquid film at the critical conditions, the fluctuations are located at the zone with a mean value of 18% of the critical film

thickness. In other words, if the film is atomized the RMS of the film thickness should be above 18% of the mean film thickness. The peak observed for the air velocities in the range of 13-15 m/s is associated with inevitable vibrations of the test section transmitted by the fun during the experimental procedure.

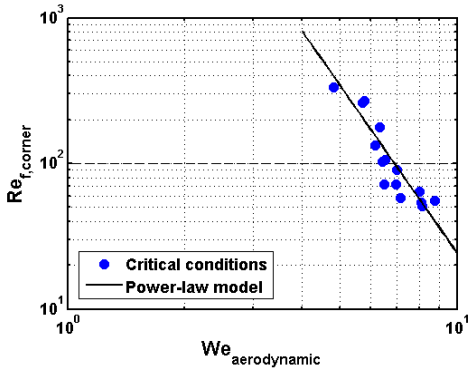

(a) Linear behavior of the critical conditions in a log-log plot.

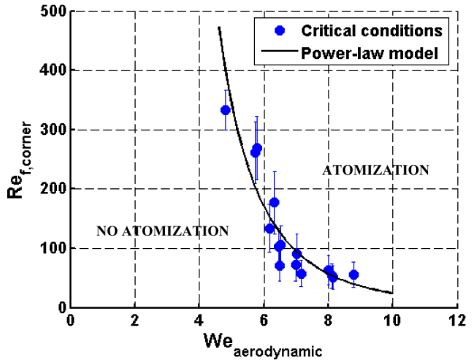

(b) Onset of atomization.

Figure 9: Critical conditions for liquid film detachment and power-law model fitted on the data.

Finally, the critical conditions for the onset of atomization of a shear-driven liquid film flowing over a horizontal plate of low surface energy, approaching a sharp corner of 90° are presented in Figure 9. They are expressed as a function of the aerodynamic Weber number ($We_{aerodynamic} = \rho_a \left(u_{air} - u_f\right)^2 h_f/\sigma_f$) which represents the ratio of the external shear to the surface tension of the film and the liquid film Reynolds number ($Re_{f,corner} = u_f h_f/\nu_f$) which expresses the inertia forces of the liquid film to the viscous ones. All the local parameters inserted in the non-dimensional numbers correspond to measurements at the edge of the flat plate. In the diagram of Figure 9b the flow conditions located at the right of the critical curve result in film atomization while tested cases at the left of the curve do not produce any atomization. A power-law model has been fitted to the experimental data in order to obtain the empirical equation of the critical curve. The formula is given below:

$$Re_{f,corner} = e^{12} \cdot We_{aerodynamic}^{-3.83} \tag{1}$$

The empirical equation is a function of the non dimensional numbers of the liquid film Reynolds and the aerodynamic Weber number. The choice of the power-law model has been dictated from the tendency observed on the experimental results in a logarithmic scale. Figure 9a shows this trend. The power-law model shows that for low external shear (low $We_{aerodynamic}$) the inertia of the liquid film has to be increased significantly in order to maintain the critical conditions while for high shear the film inertia has to become very small.

5. Conclusion

A detailed study of a horizontal shear-driven liquid film on a low energy surface approaching a sharp corner has been conducted using flow visualization techniques and PLIF measurements. The liquid film is free to expand towards the spanwise direction. The liquid film formation on the flat plate and its primary atomization depends on the ambient, initial and boundary conditions. For the conditions of this experimental work, the flow visualization study revealed different atomization regimes. An atomization map has been proposed as a function of liquid Reynolds number and air velocity. It is pointed out the way the liquid film is atomized close to the critical conditions. According to that, a disturbance created on the interface turns around the corner forming a ligament which is moving downwards and separates into a droplet after long distance from the corner.

The PLIF measurements brought light first on the characteristics of the developing film on the plate and second on the critical condition for the onset of atomization at the edge of the corner. A major difference of this horizontal film with the other ones existing in the literature is the ability to expand spanwisely. The latter influences the film formation and the atomization process at the edge of the corner. The atomization process is becoming a function of both the cross-section area of the film at the corner and the mean film velocity. Concerning the critical conditions, detailed measurements have been carried out on the liquid film.

A critical curve for the onset of liquid film separation and detachment has been determined. An empirical equation as a function of the liquid film Reynolds number and the aerodynamic Weber number fits the experimental data and describes the liquid phase detachment at the corner.

Acknowledgments

Robert Bosch Produktie in Tienen, Belgium is gratefully acknowledged by the author for the financial support of this work.

References

[1] G. B. Wallis, One-dimensional Two-phase Flow, McGraw Hill, New York, USA, 1969.

[2] N. S. Hall Taylor and G. F. Hewitt and P. M. C. Lacey, The motion and frequency of the large disturbance waves in annular two-phase flow of air-liquid mixtures, Chemical Engineering Science 18 (1963) 537–552.

[3] W. H. Henstock and T. G. Hanratty, The interfacial drag and the height of the wall layer in annular flows, AIChe Journal 22 (1976) 990–1000.

[4] J. S. Lioumbas and S. V. Paras and A. J. Karabelas, Co-current stratified gas-liquid downflow. Influence of the liquid flowfield on interfacial structure, International Journal of Multiphase Flow 31 (2005) 869–896.

[5] D. Schubring and A. C. Ashwood and T. A. Shedd and E. T. Hurlburt, Planar laser-induced fluorescence (PLIF) measurements of liquid film thickness in annular flow. Part I: Methods and data, International Journal of Multiphase Flow 36 (2010) 815–824.

[6] D. Schubring and A. C. Ashwood and T. A. Shedd and E. T. Hurlburt, Planar laser-induced fluorescence (PLIF) measurements of liquid film thickness in annular flow. Part II: Analysis and comparison to models, International Journal of Multiphase Flow 36 (2010) 825–835.

[7] P. S. C. Farias and F. J. W. Martins and L. E. B. Sampaio and R. Serfaty and L. F. A. Azevedo, Liquid film characterization in horizontal, annular, two-phase, gas-liquid flow using time-resolved laser-induced fluorescence, Experimetns in Fluids.

[8] L. A. Jurma and M. J. McCready, Study of waves on thin liquid films sheared by turbulent gas flow, Physics of Fluids A 1 (3) (1988) 522–536.

[9] S. Wittig and J. Himmelsbach and B. Noll and H. J. Feld and W. Samenfink, Motion and Evaporation of Shear-Driven Liquid Films in Turbulent Gases, Journal of Engineering for Gas Turbines and Power 114 (1992) 395–400.

[10] H. C. Kang and M. H. Kim , The relation between the interfacial shear stress and the wave motion in a stratified flow, International Journal of Multiphase Flow 19 (1) (1993) 35–49.

[11] M. A. Friedrich and H. Lan and N. E. Wilke and J. A. Drallmeier and B. F. Armaly , Measurement of the mean film thickness of dynamic shear-driven thin liquid films using optical interferometry, Atomization and Sprays 19 (7) (2009) 633–647.

[12] H. Lan and M. Friedrich and B. F. Armaly and J. A. Drallmeier, Simulation and measurement of 3D shear-driven thin liquid film flow in a duct, International Journal of Heat and Fluid Flow 29 (2008) 449–459.

[13] C. Lorencez and M. Nasr-Esfahany and M. Kawaji and M. Ojha, Liquid turbulence structure at a sheared and wavy gas-liquid interface, International Journal of Multiphase Flow 23 (2) (1997) 205–226.

[14] I. Owen and D. J. Ryley, The flow of thin liquid films around corners, International Journal of Multiphase Flow 11 (1) (1985) 51–62.

[15] B. J. Azzopardi and K. S. Sanaullah, Re-entrainment in wave-plate mist eliminators, International Journal of Multiphase Flow 11 (1) (1985) 51–62.

[16] F. Maroteaux and D. Llory and J-F. Le Coz and C. Habchi, Liquid Film Atomization on Wall Edges. Separation Criterion and Droplets Formation Model, Journals of Fluids Engineering 124 (2002) 565–575.

[17] M. A. Friedrich and H. Lan and J. L. Wegener and J. A. Drallmeier and B. F. Armaly , A Separation Criterion with Experimental Validation for Shear-Driven Films in Separated Flows, Journal of Fluids Engineering 130 (2008) 051301/1–9.

[18] J. L. Wegener and M. A. Friedrich and J. A. Drallmeier and B. F. Armaly, Experimental Evaluation of Film Separation Criterion, in: ICLASS 2009, 11^{th} Triennial International Annual Conference on Liquid Atomization and Spray Systems, Vail, Colorado, USA, 2009.

[19] P.-G. de Gennes, F. Brochard-Wyart, D. Quéré, Capillarity an Wetting Phenomena. Drops, Bubbles, Pearls, Waves, Springer-Verlag New York Inc., 175 Fifth Avenue, New York, NY 10010, USA, 2004.

[20] I. S. Carvalho and M. V. Heitoyr and D. Santos , Liquid film disintegration regimes and proposed correlations, International Journal of Multiphase Flow 28 (2002) 773–789.

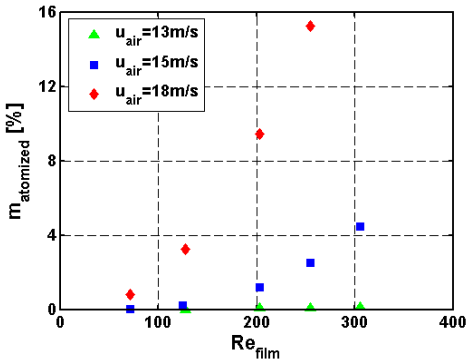

(a) Percentage of atomized mass

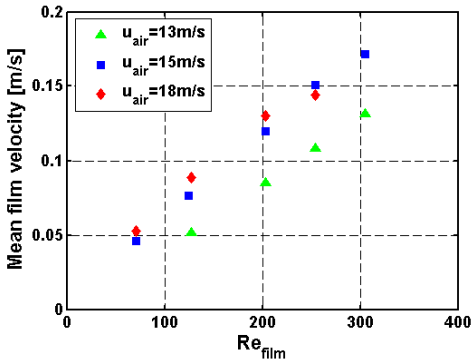

(b) Mean film velocity

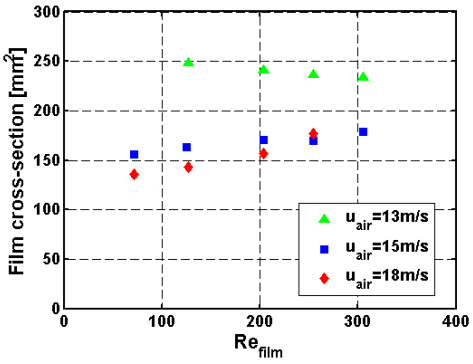

(c) Cross section of liquid film

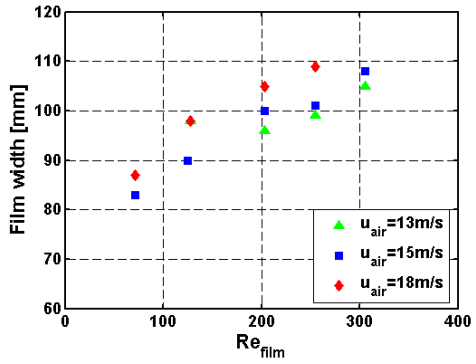

(d) Film width

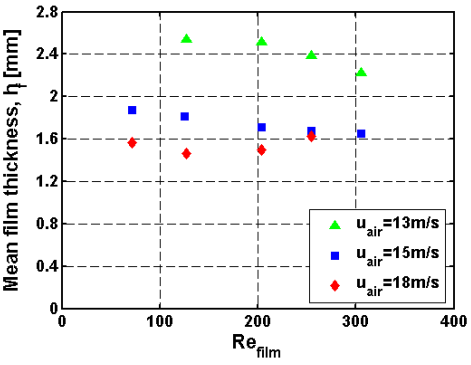

(e) Mean film thickness

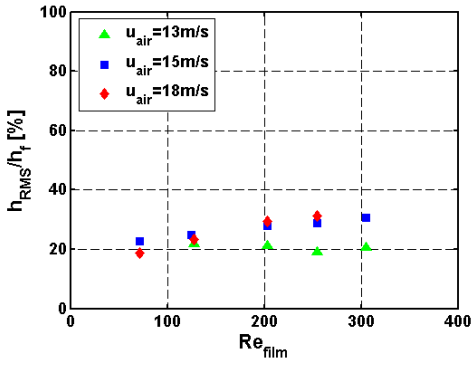

(f) Percentage of film thickness RMS

Figure 6: Atomized mass and local film characteristics measured at the edge of the corner. Case: Liquid film of region I

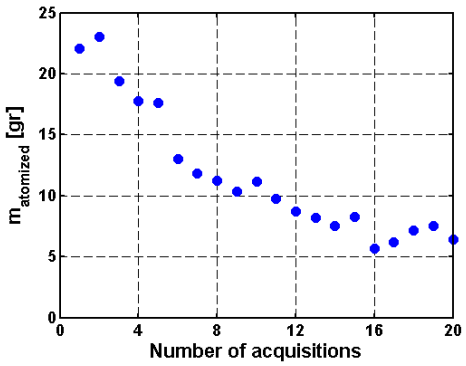

(a) Re_{film} = 254

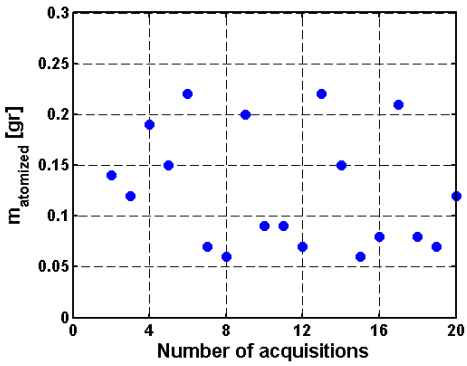

(b) Re_{film} = 117

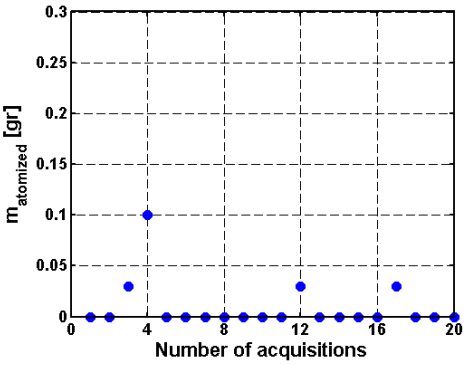

(c) Re_{film} = 97

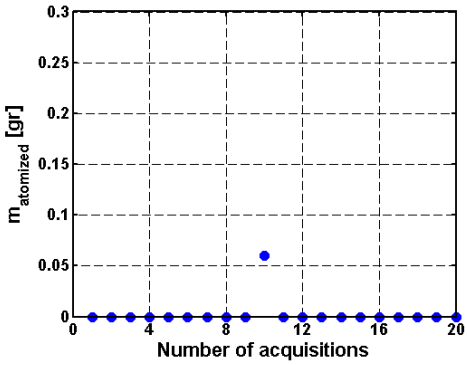

(d) Re_{film} = 86

Figure 7: Acquisitions of the atomized mass for constant air velocity u_a=15 m/s and different liquid Reynolds numbers.

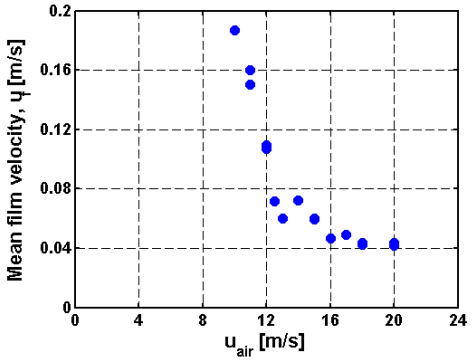

(a) Mean critical film velocity

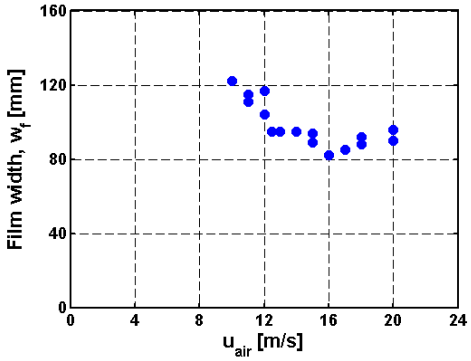

(b) Critical film width

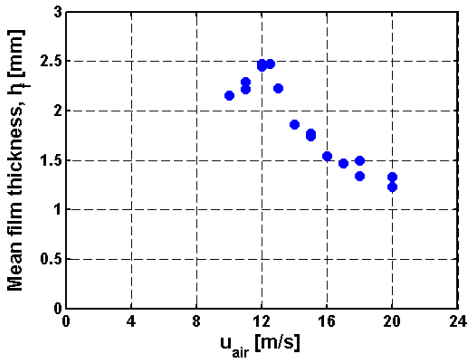

(c) Mean critical film thickness

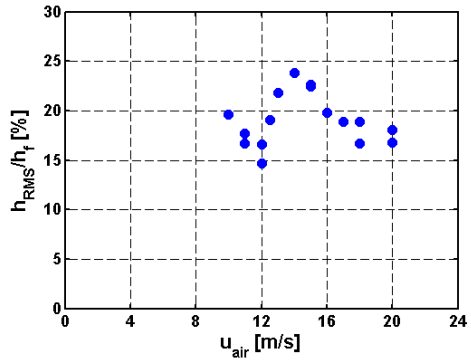

(d) Percentage of critical film thickness RMS

Figure 8: Liquid film parameters measured at the edge of the corner. Case: Critical conditions.

Development and application of the Multi Wavelength Light Extinction technique for the characterization of nano- and microparticles

Imre T. Horváth

Environmental and Applied Fluid Dynamics Department, von Karman Institute for Fluid Dynamics, Belgium, imre.horvath@vki.ac.be

Supervisor: Maria Rosaria Vetrano

Assistant Professor, Environmental and Applied Fluid Dynamics Department, von Karman Institute for Fluid Dynamics, Belgium, vetrano@vki.ac.be.

University Supervisor: Pierre Colinet

Professor, Transfers, Interfaces and Processes Department, ULB, pcolinet@ulb.ac.be

Abstract

Because of the large industrial and scientific interest in nanoparticles and nanoparticle flows, the requirement towards an online, submicron particle characterization technique is strongly expressed.

In the frame of the present PhD research a non-intrusive, optical measurement technique, the Multi Wavelength Light Extinction (MWLE) technique will be developed. It has several significant advantages compared to other existing measurement techniques. The MWLE technique is capable to measure the size distribution and concentration of the particles simultaneously, from several micrometres down to 30nm. The technique requires a simple and low-cost experimental apparatus and minimal optical access to the examined particles. These two properties make the technique suitable for online measurements in a large variety of situations. The shape of the investigated particles can be incorporated in the mathematical modeling, thus allowing the possibility for the qualitative evaluation of the particle shape, too.

The MWLE technique relies on relating the light transmittance spectrum of a particle cloud to the characteristics of the constituent particles.

The development was started with a bibliographic research on the field of light scattering by non-spherical particles. After the thorough understanding of the related theories, an appropriate mathematical model will be obtained. Two different cases will be considered; light scattering by airborne particles and particles deposited on a transparent substrate. Using the model, light scattering simulations will be carried out firstly to investigate the effect of the particle non-sphericity; secondly for the generation of the appropriate model parameters for the measurement of solid, metallic particles in both of the mentioned configurations. The retrieval of the particle size characteristics from the experimental data requires the solution of a Fredholm integral equation of the first kind, which is an ill-conditioned problem. Thus, the mathematical background of inverse problems will be studied. After, an inversion algorithm will be developed, which is robust, accurate and fast enough for the analysis of real measurement data.

After obtaining the necessary numerical and theoretical tools, the technique will be validated through the characterization of the size, concentration and fractal dimension of metallic nanoparticles and aggregates carried by a subsonic flow. The reference technique to be used will be the DMA-CPC (Differential Mobility Analyser Condensation Particle Counter) particle spectrometer. The latter investigation will be a preparation for the application of the technique in a nanoparticle production plasma facility. The aim will be to determine the particle characteristics as function of the operating parameters of the plasma facility.

The measurement technique will be further tested in the other mentioned configuration: particles deposited on a transparent substrate through the evaporation of a thin liquid layer will be examined. The prepared samples will be analysed by SEM (Scanning Electron Microscope), in order to provide a proper validation of the size analysis capabilities of the technique.

Keywords: nanoparticle, particle size distribution, light extinction, inverse problem, regularization

Experimental Study and Modeling of Two-phase Flow Cavitation and Flashing through Complex Valves

Jorge Pinho

Environmental and Applied Fluid Dynamics Department, von Karman Institute for Fluid Dynamics, Belgium, jorge.pinho@vki.ac.be

Supervisor: Patrick Rambaud

Associate Professor, Environmental and Applied Fluid Dynamics Department, von Karman Institute for Fluid Dynamics, Belgium, rambaud@vki.ac.be

Promotor: Jean-Marie Buchlin

Professor, Head, Environmental and Applied Fluid Dynamics, von Karman Institute for Fluid Dynamics, Belgium, buchlin@vki.ac.be

Industrial Supervisor: Saïd Chabane

CETIM, Centre Technique des Industries Mécaniques, France

Abstract

Two-phase flow are widely present in nuclear, chemical or mechanical engineering where different gas-liquid reactors, boilers, condensers, evaporators and/or combustion systems can be found. In these hydraulic systems the use of mechanical valves has a preponderant role for the security as it represents the ultimate protection before an accident. The complete understanding of the physics taking place in the flow through a valve becomes therefore crucial to guaranty this security of the protected process. In nuclear or thermal engineering systems the use of safety relief valves (SRV) is mandatory since it protects them against any over pressures. A careful design of the SRV is therefore essential. Reliable methods are available for SRV design in the cases of single phase flow such as liquid or gas discharge. When the static pressure through the valve falls below the liquid saturation pressure, vapor bubbles will form which tend to reduce the medium sound velocity. Similarly to compressible flow, this decrease of the speed of sound will be linked to limitation of the mass flow rate evacuated. In this two-phase flow, the single phase design methodology becomes inadequate. Currently, there are some calculation methods that attempt to predict the critical flow onset in SRV for two-phase systems knowing the inlet flow conditions and the outlet pressure; however none of them are acknowledged as being fully reliable as they make use of void fraction that is not currently measurable for flow experiencing cavitation.

This research project will be carried out at the von Karman Institute for Fluid Dynamics (VKI). A previous work carried out by Vasilis Kourakos focused on a two-phase flow through a SRV when air was injected upstream the valve. Several studies were performed and comparison with a transparent model was carried out at ambient temperature in an open loop. This previous work did not consider the case in which the fluid cavitates and/or flashes itself, being the reason why an external source of air was indeed needed to promote a two-phase flow.

The first part of the present research project is to update the VKI facility in order to increase the operational temperature and control the SRV back pressure. The new experimental facility will include a closed loop. Test conditions will be set through the control of a parallel pressurizing and vacuum system. Typically for water at 50C, cavitation will occur when the static pressure will fall below 12.3KPa.

Used measurement techniques will include; flow visualizations with a high-speed camera; unsteady pressure measurements upstream, inside and downstream the valve; temperature measurements; and void fraction measurement. This last technique will require a dedicated development. The proposed methodology consists in measuring the local sound velocity to retrieve the local void fraction. Proper calibration will have to be developed as well. Once knowing the void fraction in cavitation or flashing mode, the model predicting the mass flow rate such as the HNE-DS (2004) will be validated for the first time in this configuration.

Keywords: Two-phase flow, cavitation, flashing, safety relief valve, discharge coefficient

Experimental Study of Buoyant Plume and Thermal Stratification in a Liquid Metal Nuclear Reactor

Chiara Spaccapaniccia

Environmental and Applied Fluid Dynamics Department, von Karman Institute for Fluid Dynamics, Belgium, chiara.spaccapaniccia@vki.ac.be

Supervisor and University Supervisor: Jean-Marie Buchlin

Professor, Environmental and Applied Fluid Dynamics Department, von Karman Institute for Fluid Dynamics, Belgium, buchlin@vki.ac.be

Professor, Faculté de Sciences Appliquées, Université Libre de Bruxelles, Belgium, buchlin@vki.ac.be

Abstract

The development of new generation liquid metal cooled reactors leads to numerous advantages in the nuclear energy technology, such as a higher power density and improved operating safety.The Belgian nuclear research institute (SCK¢CEN) is developing MYRRHA, a subcritical liquid metal cooled reactor and commissioned at VKI the construction of a scaled water model.

One of the aspects to be tested is the formation of a stratified buoyant plume establishing during the reactor shut-down in the above core region that may influence the heat removal in natural convection working conditions and affect the integrity of the system. The thermal stratification of the plume anticipated in such a transient and the magnitude of the upper plenum thermal gradient should be assessed as a function of the core decay power.

The experimental techniques proposed for the analysis of the transient are the Particle Image Velocimetry and the Laser Induced Fluorescence: the PIV technique will be used for the measurement of the velocity field, while the thermal field will be measured by LIF.

The use of planar optical techniques for velocity and temperature measurements leads to numerous advantages. They can be used simultaneously, as required by the analysis of transient flows. They can picture complex phenomena like the thermal stratification of a buoyant plume . Furthermore the simultaneous measurements of the velocity and temperature fields allows the establishment of fine correlations between the buoyancy driven convective motion and the heat transfer mechanisms.

Before applying the proposed analysis to the water model of the whole MYRRHA reactor the combined PIV and LIF will be tested in step by step increasing complexity models.

The simultaneous application of PIV and LIF technique will be first assessed for natural convection cases by performing measurements on a vertical square enclosure uniformly heated in one side and uniformly cooled the other side thanks to the use of two Peltier elements. This model is chosen for the large availability of experimental and numerical data in literature. The aim is to determine which are the best seeding conditions for natural convection PIV test in water and the dye concentration that allows the highest temperature resolution obtainable through one color LIF.

A further step is the application of the proposed experimental study on the upper plenum of a small two dimensional natural convection model (Aquarium). The loop is designed in order to respect as much as possible the similarity with the MYRRHA hydraulic circuit working in natural convection conditions. The loop includes a heating section where a buoyancy plume develops and produces a thermal stratification in the upper plenum and a cooling section. The overall effect is a mass flow driven only by natural convection (Thermosyphon loop). The tests on the model will allow to validate the experimental techniques chosen and confirm the adequacy of their application for the analysis of stratification in the large scale model. Moreover they will allow to achieve a better understanding of the parameters that could influence the thermal stratification in the upper vessel region, such as the upper plenum geometry, the presence of obstacles in the above heat source region and the power distribution in the heat source.

Development of a Numerical Simulation Tool for the Aerothermal Flow through an Ablative Thermal Protection System for Atmospheric Entry

Pierre Schrooyen

Aeronautics and Aerospace Department, von Karman Institute for Fluid Dynamics, Belgium, pierre.schrooyen@vki.ac.be

Supervisor: Thierry Magin

Assistant Professor, Aeronautics and Aerospace Department, von Karman Institute for Fluid Dynamics, Belgium, magin@vki.ac.be

University Supervisor: Philippe Chatelain

Assistant Professor, Institute of Mechanics, Materials and Civil Engineering, Université Catholique de Louvain, philippe.chatelain@uclouvain.be

Keywords: atmospheric entry, thermal protection system, ablation, pyrolysis, laminar-turbulent flow transition.

1. Introduction

The challenge of atmospheric entry for a spacecraft has stimulated research on the aerothermal flow around the vehicle Thermal Protection System (TPS). During this phase, the spacecraft is strongly affected by aerodynamic heating due to the dissipation of its kinetic energy. Predicting an accurate heat-flux is a complex task, and especially modeling the following phenomena that are potential mission killers: the complex surface chemistry on the thermal protection material and the flow transition from laminar to turbulent. These difficulties are enhanced at higher entry velocities, typical of new missions to Mars or asteroids. To protect the payload or the astronauts onboard, engineers use safety factors to design the heat shield thickness leading to increased mass of the TPS.

The experimental investigation of entry aerothermal problems is still an extremely difficult endeavor which makes numerical methods crucial in advancing our understanding of these phenomena and in developing predictive design tools.

2. Problem statement

Reusable and ablative materials are the two main types of TPS in use today. While reusable protection materials are designed for low heat flux trajectories, ablative TPS are best suited for high entry velocity [1]. Requirements concerning mass efficiency for missions with very high entry velocities have led to the development of a new class of light carbon composite ablators. The components of these materials are carbon fibers and a filler matrix of phenolic resin. During atmospheric entry, a part of the heat flux is transferred inside the heat shield, leading to a gradual temperature increase of the material and to its transformation. One can separate the TPS in different zones: the virgin material, the pyrolysis zone and the char layer (see Fig. 1).

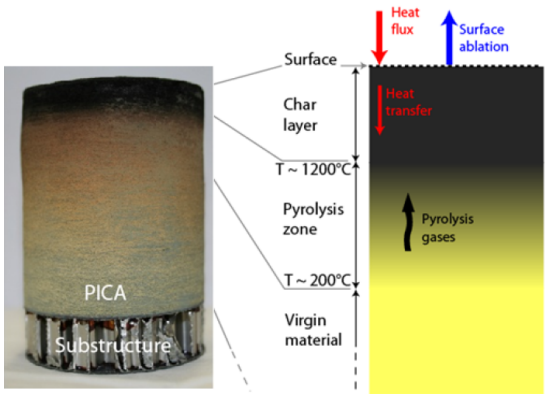

Figure 1: Picture of a core of Phenolic Impregnated Carbon Ablator (PICA) extracted from the TPS of Stardust [2] and schematic of the zones of degradation illustrating the material response to high-enthalpy flow

The virgin material is the unaltered part of the shield. In the pyrolysis zone, the phenolic resin is

progressively carbonized producing pyrolysis gases which are transported out of the material by diffusion and convection through the pores. The third zone is composed of the fibrous carbon preform and of the carbonized phenolic resin and is destroyed by ablation [3].

The models implemented until recently are well suited for dense ablative materials but for this new class of material, new design tools need to be developed. Our poor understanding of the coupled mechanisms of ablation and flow transition leads to difficulties in heat-flux prediction. More specifically, pyrolysis and ablation generate a mass flow and a surface roughness that interact with the flow in the boundary layer. Such perturbations can trigger transition of the flow from laminar to turbulent, leading to a strong increase of the convective heat-flux. This interaction between the type of flow and the roughness is illustrated in Fig. 2.

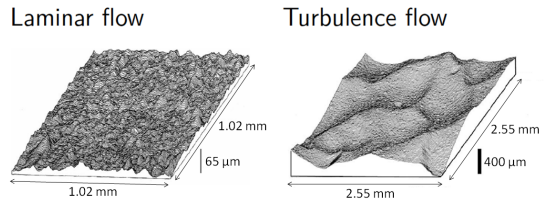

Figure 2: Surface topographies of polycrystalline graphite samples ablated under different flow regimes [4].

3. Method

The objective is to develop an integrated numerical tool for the high-fidelity prediction of the aerothermal performance of light carbon composite materials and their effects at the scale of the vehicle. This work focuses on the combined simulation and modeling of the flow and wall phenomena by means of a computational approach that can go seamlessly from a compressible flow to porous media and implements the most accurate physical models for non equilibrium flows and ablation. Accordingly, the goal is to capture the flow features away from the wall, the developing boundary layer, and the phenomena inside the TPS material. The challenges are many. Not only does one need to correctly resolve these two distinct media, the open flow and the wall but it is quite critical to capture their interactions and in particular the balance of the phenomena in the context of the transition of the boundary layer from laminar to turbulent regime.

The numerical tool will be implemented inside an existing code Argo developed in Cenaero. This platform is based on a Discontinuous Galerkin Method (DGM) which cumulates the advantages of finite volume and finite element discretization [5]. The approach will consider both the Direct Numerical Simulation (DNS) of the fluid flow equations for simplified geometry and their solution through modeling in a spatially filtered context (Large Eddy Simulation-LES). DGM is well suited for DNS and LES for complex geometry thanks to the use of unstructured meshes. Argo already possesses a formalism to solve convection-diffusion-reaction problem as well as an implicit temporal integration. This platform has already proven its capability to run DNS and LES computation in parallel for transitional flow at relatively high Reynolds number (60-100) [6].

The implementation strategy of the different models for the porous media follows the approach proposed by Lachaud to develop the Pyrolysis and Ablation Toolbox based on OpenFOAM (PATO) [7]. In a first step, we will consider the implementation of the model of Kendall et al [8] published in 1968 which has proved its validity for dense material. From the extremely complex phenomena occurring in a porous ablative material, they are only modeling Fourier's heat transfer and pyrolysis of the solid. Progressively more complex models will be introduced which take into account, for example, the identification of the species produced by pyrolysis, the transport and the chemical evolution of the pyrolysis gases inside or outside the material or the ablation as a volume phenomenon.

The verification and validation of the numerical tool developed will be gradual in its complexity and complementary by the different aspects tested. For instance, a milestone of the project is the comparison of the results with the work of Crocker and Dubief [9] which deals with a turbulent flow in a channel influenced by an eroding wall. Comparisons with simple geometry test cases studied at the Université catholique de Louvain in pyrolysis of the biomass and VKI experimental data will allow to validate the simulations inside the heat shield.

4. Ongoing work

Our current effort is twofold. On one hand, we focus on the implementation of diffusive and reaction

terms in a one dimensional DG code. On the other hand, we investigate immersed interface techniques for moving boundaries in a DG context in order to capture recession of the material. The results of the current 1D code are compared with the Aerotherm Charring Material Ablation (CMA) program developed by Kendall et al [8].

5. Perspectives

The numerical methods currently being implemented will be useful to compare against the results of Crocker and Dubief [9] . In this context, we envisioned to use immersed interface technique to model surface ablation. According to the assumptions of Kendall et al [8], the flow of pyrolysis gas through the TPS is considered normal to the heated surface and the drop in pressure through the char is supposed negligible. The next step will be to drop this hypothesis and solve Darcy's equation which models the gas flow inside the porous medium. Afterwards, the idea is to evolve towards 2D and 3D versions of the code describing the in-depth thermal response of the material.

Acknowledgments

The author acknowledges support through a fellowship from the "Fond pour la formation à la Recherche dans l'Industrie et dans l'Agriculture "and support of the Argo team from Cenaero.

References

[1] J. A. Dec, Three Dimensional Finite Element Ablative Thermal Response Analysis Applied To Heatshield Penetration Design, Ph.D. thesis, Georgia Institute of Technology (2010).

[2] M.Stackpoole and S. Sepka and I. Cozmuta and D. Kontinos, Post-flight evaluation of stardust sample return capsule forebody heat shield material, in: paper AIAA 1202, Aerospace Sciences Meeting and Exhibit, Washington, DC, 2008.

[3] J. Lachaud, T. Magin, C. I., N. Mansour, A short review of ablative material response models and simulation tools, in: 7th European Aerothermodynamics Symposium, Brugge, 2011.

[4] G. Vignoles, J. Lachaud, Y. Aspa, J. Goyhénèche, Ablation of carbon-based materials: Multisclae roughness modelling, Composites Science and Technology 69 (2008) 1470–1477.

[5] J. Hesthaven, T. Warburton, Nodal Discontinuous Galerkin Methods; Algorithms, Analysis and Applications, Text in Applied Mathematics, Springer Verlag, 2008.

[6] K. Hillewaert, Convergence analysis of higher-order discontinuous galerkin method for the direct numerical simulation of transitional flows, in: DEISA PRACE Symposium 2011, Stockholm, 2011.

[7] J. Lachaud, A pyrolysis and ablation toolbox based on openfoam, in: 5th OpenFOAM Workshop, Chalmers, Gothenburg, June 21-24, 2010.

[8] E. P. Bartlett, R. M. Kendall, An analysis of the coupled chemically reacting boundary layer and charring ablator. part 3 - nonsimilar solution of the multicomponent laminar boundary layer by an integral matrix method, Contractor Report CR-1062, NASA (1968).

[9] R. Crocker, Y. Dubief, Numerical study of turbulence over a receding wall by controlled and thermal ablation, in: Proceedings of the Summer Program 2010, Center for Turbulence Research, Stanford, USA, 2010.